Fermi National Accelerator Laboratory

FERMILAB-Pub-82/43
8055.000
(Submitted to Nucl. Inst. Meth.)

CALCULATION OF ANTIPROTON YIELDS FOR THE FERMILAB ANTIPROTON SOURCE

Carlos Hojvat and A. Van Ginneken

Fermi National Accelerator Laboratory
Batavia, Illinois 60510

July 1, 1982

Abstract

The available experimental data for antiproton production are described by an analytical formula, including target nucleus dependence. This formula, in conjunction with a Monte Carlo program that includes the effect of hadronic showers, is used to optimize the design of the Fermilab Antiproton Source. Comparison is made with measurements of yields at the CERN Antiproton Accumulator.

Operated by Universities Research Association Inc. under contract with the United States Department of Energy

1. Introduction

Due to developments in beam cooling techniques it is now possible to accumulate antiprotons ($\bar{p}$) in sufficient numbers within phase space areas compatible with utilization in accelerators. The possibility of increasing the phase space density of antiprotons is a direct result of the development of electron cooling techniques by Budker[1] and the invention of stochastic cooling by van der Meer.[2] Intense bunches of $\bar{p}$ can be made to collide with proton bunches in colliding beam machines with large gains in center-of-mass energy over collisions with stationary targets. Several laboratories have proposed such facilities.[3] At the CERN SPS accelerator experiments which study 270 GeV $\bar{p}p$ collisions have recently started.[4]

This report summarizes a set of calculations on antiproton production in complex targets for aiding in the design of the Fermilab Tevatron I Antiproton Source. The emphasis is on the optimization of the accumulation rate of antiprotons to maximize the expected peak and average luminosity of the $\bar{p}p$ collisions in the Tevatron accelerator. Although several other calculations[5] exist a comparison is presently not attempted.

The calculations rely on the Monte Carlo (MC) program CASIM.[6] This program generates three dimensional nuclear cascades. Antiproton production by all members of the cascade is included, along with the subsequent transport of the $\bar{p}$ through the target and collection devices. An empirical fit to

available data of $\bar{p}$ production is introduced into the program expressly for this study. This fit is described below, along with a brief sketch of its implementation into CASIM.

The CERN Antiproton Accumulator has now been in operation for some time. It provides the opportunity of comparing expected $\bar{p}$ yields from the present calculations with actual measurements for that specific geometry. Such comparisons are made below.

This report is divided in seven sections. Section 2 contains the model for $\bar{p}$ production. Section 3 discusses its adaptation to the MC code CASIM. The results for the Fermilab parameters are given in Section 4 and the comparison with CERN data in Section 5. Section 6 contrasts the differences between Fermilab and CERN designs.

2. Antiproton Production Cross Section

The calculation of $\bar{p}$ yields relies on the production cross section not only for beam protons (primaries) but also for particles participating in the shower development (secondaries). In the present calculation the secondaries considered are p, n, π^+, π^-, and $\bar{p}$. Production of $\bar{n}$ which may subsequently transform to $\bar{p}$ via charge exchange (including inelastic charge exchange, i.e., transformation of a leading particle) is not considered explicitly. To first order this

process and its (likewise neglected) inverse are expected to compensate each other.

For nucleons and pions incident on protons as well as on nuclear targets the available data are described by an empirical formula which factors into three parts:

(i) a fit to data[7] in the (high energy) scaling region,

(ii) a factor describing the approach to scaling at lower incident energies, and

(iii) the nuclear mass dependence.

The scaling variables chosen are the transverse momentum, p_t, and the radial scaling variable, $x_R (\equiv E/E_{max}$, the $\bar{p}$ energy in the center of mass expressed as a fraction of its largest kinematically allowed value). It has been shown[8] that x_R has better scaling properties, especially at lower incident energies, than the more conventional Feynman x.

The empirical formula for the invariant $\bar{p}$ production cross section (divided by the target absorption cross section) with the three factors separately bracketed is given by:

$$(E/\sigma_{abs})(d^3\sigma/dp^3) =$$

$$[k(1-x_R)^m \exp(-3p_t^2)].$$

$$[1+24s^{-2} \exp(8x_R)].[a \exp(bp_t^2) \exp(-cx_R)] \qquad (1)$$

where σ_{abs} is the absorption cross section of the target

nucleus. The projectile dependent constants k and m are given in Table I. The target dependent constants and a, b, and c are given in Table II for five elements. For other materials the constants are obtained by interpolation. The cross section is assumed to vanish abruptly at the kinematical limit for $\bar{p}$ production on a proton target. Some subthreshold production in nuclear targets aided by Fermi motion is thereby ignored.

From Equation (1) it can be seen that the fit in the scaling region follows a familiar form. The approach-to-scaling factor is based on very few data and therefore not well established. It is not significant in the Fermilab case (e.g., for 120 GeV/c protons producing $\bar{p}$ near x=0, the factor is 1.004), although it is somewhat more important for the CERN case (at 25 GeV/c, the comparable factor is 1.13 and at 15 GeV/c it is 1.96). Note from these examples and from Equation (1) that scaling is approached "from above" in accordance with Reference 8.

The factor describing the nuclear effects also contains some uncertainties. This is especially true for backward production in the center of mass where the cross section might be enhanced as is observed for total hadron production.[9] The expression in Equation (1) is exclusively based on forward $\bar{p}$ production in the c.m. Some of the uncertainty about backward production is removed by computing the $\bar{p}$ yield following two different prescriptions. The first assumes symmetric c.m. $\bar{p}$ production for all nuclear targets. The second prescription

starts from a simple formula of Brodsky et al.[10] which predicts the ratio of total hadron production off nuclei to that off protons as a function of the rapidity variable. This formula is used here only to predict forward-to-backward ratios of $\bar{p}$ production on nuclear targets, with forward production taken from Equation (1). It can be argued on kinematical grounds that this second procedure overestimates any nuclear enhancements. These computations show that even with such an enhancement, backward produced $\bar{p}$ are not likely to be of great interest in this study. In addition, recent results[11] not included in the data basis of Equation (1) show no significant enhancements to be present at 70 GeV, even for heavy nuclei. For these reasons, all results quoted below assume $\bar{p}$ production to be symmetric in the center of mass.

Both approach-to-scaling and nuclear mass dependence are based on proton projectile data only. For incident pions they are assumed to be equal to the proton case. For backward $\bar{p}$ production by incident pions the constants k and m in Table I are taken to be those for proton projectiles. This leads to unphysical discontinuities in the cross section and in its slope at x=0 which are tolerated for simplicity.

Production of $\bar{p}$ by inelastic collisions of $\bar{p}$ is assumed to follow the leading proton distribution of the Hagedorn-Ranft model[12] for p-nucleus collisions. This is for convenience since this model is already coded into CASIM.

A thorough statistical evaluation of the quality of the fit of Equation (1) to the data is not attempted. The presentation is limited to three projections of the fit, with special attention to the low p_t, low x region of interest here. The data are projected onto the graphs by applying a correction to the cross section using Equation (1). Information from the fit outside the plane of the graph is thereby introduced. The comparison is obviously more significant if such corrections are reasonably small and uniform. For this reason as well as for clarity of the graphs, the sample of data included is somewhat restricted. Comparisons are shown for proton projectiles on hydrogen and lead targets.

Figure 1 shows the dependence on incident proton momentum with $p_t=0$ and x=0 held constant. The steep rise in the cross section is primarily the result of the decrease in x_R with s at constant x=0:

$$(x_R)_{x=0} = 2m\sqrt{s}/(s-8m^2) \qquad (2)$$

where m is the proton mass. At low incident momentum there is also a significant contribution to the rise from the approach-to-scaling factor. Figure 2 presents a fit of the x_R dependence with $p_t=0$ held constant and $s\rightarrow\infty$. In both Figures 1 and 2 the correction factors vary from unity to about seven but are mostly in the lower part of that range. Figure 3 shows the p_t dependence with $x_R=0$ held constant and $s\rightarrow\infty$. Note that $x_R=0$ is always in the unphysical region of Equation (1). The

correction factors are very large here (up to 10^4), mainly due to the projection onto x_R=0. Note also in Figure 3 that the scale of the cross section is greatly expanded.

It should be noted that Equation (1) is an attempt at fitting a set of data from different experiments in an unbiased way. Some peculiar consequences of this might be seen in Figure 3 where the fit underestimates the hydrogen data of Allaby et al. but overestimates the data for lead of the same experiment. A somewhat similar inversion exists with respect to the data of Dekkers et al., though not in as uniform a fashion. A critical evaluation of the data might suggest a set of weights to be applied in constructing the fit. This is not attempted here.

It must be emphasized that Equation (1) is expected to be more accurate for small p_t ($\lesssim$1 GeV/c) and small to moderate x_R($\lesssim$.75), which is the region of interest for the present application.

The $\bar{p}$ yield for a given target and collection device, depends on many variables in addition to those of Equation (1). It is the purpose of the MC program to include these variables in the analysis. However, as an intermediate step it appears useful to present graphs of cross sections based on Equation (1) and simple integrals thereof. Figure 4 presents the differential cross section in the laboratory, $dN/dpd\Omega$, evaluated in the forward direction versus $\bar{p}$ laboratory momentum for a number of incident proton momenta on a tungsten target.

Figures 5 and 6 show total $\bar{p}$ production per interacting proton on tungsten below 30 mrad and 60 mrad respectively as a function of $\bar{p}$ laboratory momentum for the same set of incident energies. Figures 7 and 8 present the total $\bar{p}$ production per interacting proton on tungsten below p_t of 0.3 GeV/c and 0.6 GeV/c, respectively, again for the same range of $\bar{p}$ momenta and the same set of incident momenta. In all these graphs the results at very low $\bar{p}$ momenta ($\lesssim$2 GeV/c) are suspect because the procedure of symmetrizing the cross section about x=0 on a nucleus does not take account of the influence of Fermi motion of the target nucleons.

3. Monte Carlo Calculation

The purpose of this calculation is to obtain the expected $\bar{p}$ yield for specific geometries of production and collection. It incorporates the fit to the $\bar{p}$ cross sections described in the previous section as well as all relevant details of a particular collection geometry.

The physical model of the calculation is essentially that used in the MC code CASIM.[6] Particle production in CASIM is based on the Hagedorn-Ranft[12] model. Though somewhat outdated, its predictions agree well with experiment in the regime of interest here. In CASIM a hadron shower is composed of only nucleons and pions. Effects of other hadrons which can

participate in the cascade are not outright neglected since energy conservation is enforced (in the mean) among the nucleon and pion members. For the present study this model must obviously be supplemented by some information on $\bar{p}$ production and transport.

Production of $\bar{p}$ is represented in the program by Equation (1). The (stepwise) transport of $\bar{p}$ is like that of protons in CASIM and includes multiple Coulomb scattering, ionization loss and coherent as well as incoherent nuclear elastic scattering. Above 50 GeV the $\bar{p}$ absorption cross section is assumed constant and equal to that of protons. Below 50 GeV the $\bar{p}p$ cross section is known to grow with decreasing energy. For hydrogen this energy dependence is taken from experiment.[13] For nuclear targets it is derived from $\bar{p}p$ data plus a simple geometrical model of the nucleus.[14] The enhanced cross sections at lower energy are due to $\bar{p}$ annihilation. It is assumed that the ratio of annihilation to total cross section is independent of nuclear species.

As in CASIM a shower is initiated by an incident particle selected from a prescribed beam distribution. This particle is forced to interact in the target and collection system and a representative shower particle is then traced through the target and focusing elements. The representative members of this shower are called <u>propagating</u> particles and are themselves not subject to analysis. From each vertex of this shower one or more particles are generated and then traced through the

target system. Upon emergence they are analyzed for their contribution to various distributions. These are called recording particles and in the present problem all are $\bar{p}$.

In addition to $\bar{p}$ generation by nucleon and pion members of the shower one extra mode of production is explored, i.e., leading particle $\bar{p}$ resulting from $\bar{p}$ inelastic collisions. For this reason $\bar{p}$ are included among the propagating particles. To obtain a statistically meaningful sample of such event chains, selection of $\bar{p}$ is enhanced by several orders of magnitude as compared with the actual production probability. The low weight thereby incurred is offset by the increased probability to produce a (leading) $\bar{p}$. Annihilation of $\bar{p}$ is included on an averaged basis, i.e., by reducing the outgoing $\bar{p}$ weight by the annihilation probability of the incident $\bar{p}$.

The recording particles (exclusively $\bar{p}$) are selected with a momentum chosen uniformly within the accepted range plus the expected ionization loss. The number of such $\bar{p}$ generated at each vertex depends on the incident particle type. It varies from one to five and is empirically determined such as to roughly minimize the statistical error in total $\bar{p}$ yield. The angle of the $\bar{p}$ with respect to the projectile is chosen from a Gaussian distribution with standard deviation dependent upon depth in the target system. The $\bar{p}$ so generated are traced through the target and collection devices to the downstream end of the system. They are then projected onto a conveniently located aperture plane where they are either analyzed on-line

or listed on a file for later use, e.g., in a beam transport code. The recording $\bar{p}$ undergoes elastic processes in stochastic fashion during transport but absorption is taken into account on the average, i.e., by reducing the weight at each step.

The typical step size selected for transport of both propagating and recording particles is 0.2 cm. Sensitivity to the focusing process in the collection devices precludes substantially larger steps. Typically, the $\bar{p}$ yield is calculated to within a few percent (statistical errors only). Most MC runs for this problem use correlated sampling of the random number sequences to help reduce relative errors between runs which differ only slightly in beam size or dispersion, geometry, target composition, magnetic field, etc.

The MC program lists the $\bar{p}$ yield as a function of acceptance for each of a set of values of the aspect ratio of the acceptance cut ellipses. The yield is further separated according to whether the $\bar{p}$ originates from primary interactions, secondary nucleons, pions, or $\bar{p}$. In addition, a selected number of histograms and scatter plots are produced. The histograms include yield as a function of production angle and of phase space acceptance as well as of the depth and radius of $\bar{p}$ origin within the target. The scatter plots display the $\bar{p}$ yield as a function of x-y position at production and of transverse phase space (at the acceptance cut plane as well as projected back to the center of the target). Some

histograms and plots are presented separately for primary and secondary production and for a set of fixed values of the acceptance cuts.

4. Fermilab

4.1 Choice of Parameters

As seen in Figures 4 through 8 the $\bar{p}$ yield increases with increasing primary proton energy. Both the optimum $\bar{p}$ momentum and the optimum yield increase almost proportional to the incident proton energy.

Once the Tevatron and the Colliding Beam Facility are commissioned the highest Main Ring energy is expected to be 200 GeV. The maximum energy which can be extracted at a medium straight section is 120 GeV. Extraction at the Main Ring medium straight section F17 offers a convenient location for both target station and Antiproton Source within the Fermilab complex. Therefore, while a higher $\bar{p}$ yield may be obtained with 200 GeV protons, the convenience of the F17 location plus the expected lower operating costs support the choice of 120 GeV for the incident proton energy.[15]

For the above primary proton energy, 90% of the optimum yield can be obtained for $\bar{p}$ momenta between 8.5 GeV/c and 16.5 GeV/c. The accumulation process of $\bar{p}$, requiring compression of their 6-dimensional phase space, or "cooling", favors a lower

antiproton momentum. Since the normal Main Ring injection momentum of 8.9 GeV/c is within the yield plateau, this seems to be an obvious choice for the $\bar{p}$ energy. Antiprotons can be injected back into the Main Ring after accumulation and cooling, without pre-acceleration.[15]

As presently envisaged the Antiproton Source can effectively accomodate a total longitudinal $\bar{p}$ momentum spread of less than 4%. In calculating the yields, this variation in momentum is included. For small momentum spreads the yield of $\bar{p}$ can be assumed to be directly proportional to the range of longitudinal momenta accepted. However, for any finite acceptance the number of $\bar{p}$ actually transmitted will not increase in the same proportion due to chromatic effects. The present calculations include only chromatic effects of the $\bar{p}$ collecting system.

The collection of antiprotons assumes the utilization of a lithium lens.[16] The advantages of an element focusing simultaneously on both planes are self-evident. In addition the very short focal distances that can be obtained result in very small chromatic effects. The merits of a lithium lens to adapt the phase space of $\bar{p}$ emerging from the target to a beam transport system have been already discussed.[17] Based on the experience at the INP, Novosibirsk, USSR,[18] the collection lens is taken to be a lithium lens of 1 cm radius, a magnetic field gradient of 1000 Tm^{-1} and a length of 15 cm. For such a lens and for a $\bar{p}$ momenta of 8.89 GeV/c the distance between focal

plane and the lens entrance surface (f*) is 14.45 cm. The center of the target is assumed to be at the upstream focal plane unless otherwise indicated. As part of the optimization procedure lenses of larger radius or larger gradients are considered. The advantages of a short focal length collector are best exploited by the use of high density targets to offset the depth-of-focus effect by concentrating the production of $\bar{p}$ in as short a length as possible.

The antiproton collection system imposes a maximum angle within which antiprotons can be collected. The area in phase space over which the antiprotons are produced is then determined by the apparent size at the target of the source of antiprotons, i e., the proton beam size. Therefore, the density of $\bar{p}$ in phase space increases with decreasing proton beam size until multiple scattering and secondary production essentially decouple the apparent size of the source of $\bar{p}$ from the actual proton beam size. A higher $\bar{p}$ density in phase space requires less cooling and reduces the accumulator aperture needed to achieve a given final $\bar{p}$ density. The minimum proton spot size which can be utilized is limited by the energy density deposited in the target. Energy densities in excess of 200 Joules . gm^{-1} are expected to result in target failure and density depletion resulting from shock waves propagating through the target.[19] Among high density materials tungsten (and its rhenium alloys) have good mechanical properties at elevated temperatures. A study of the energy density deposited

by a 120 GeV proton beam in tungsten is performed with the program CASIM.[5] The maximum of the deposited energy density, E_D, within a 5 cm long tungsten target is shown in Figure 9 as a function of σ, the rms size of the proton beam (assumed equal for the x and y dimensions). It is assumed that the protons are incident on the target over a time interval short compared with thermal diffusion times. It is seen that E_D follows closely a σ^{-2} dependence. From the value of E_D for a given σ, the maximum number of protons, N_p, that can be targeted so as not to exceed locally the amount of 200 J gm^{-1} is also shown in Figure 9. For beam intensities of about 3×10^{12} protons/pulse, σ of about 0.04 cm are indicated. Schemes involving rapid sweeping of the proton beam and the $\bar{p}$ acceptance channel, have been proposed to eliminate this limitation.[20]

A summary of the parameters discussed above for the Fermilab geometry is given in Table III. The geometry of the target region and collector lens is shown in Figure 10.

4.2 Results

Antiproton yields are calculated for a range of parameters in order to optimize their collection. Yields are typically quoted as number of antiprotons per GeV/c of longitudinal momentum acceptance and per incident proton.

The incident proton beam is assumed to have a circular waist at the center of the target. The beam distribution are described with Gaussians in each of the four transverse dimensions. The normalized proton beam emittance (containing 95% of the beam) is assumed to be $24\pi\times10^{-6}$ mrad.[21] Beam sizes are quoted by their transverse σ(rms) size.

By choosing the aperture plane to be the second focal plane of the lithium lens, particle distributions are essentially symmetric with respect to the transverse phase space coordinates. On this aperture plane, machine acceptances representing the aperture of the Antiproton Source assumed equal in both transverse phase spaces are imposed with upright ellipses. The aspect ratio of these ellipses is varied to obtain the maximum $\bar{p}$ yield for a given acceptance and always these optimum values are quoted.

For the standard parameters of Table III a subset of the distributions obtained from the MC program is presented. Figure 11 shows the distribution of all $\bar{p}$ generated as a function of their production angle with respect to the (central) proton beam direction. The only cut is that imposed by the outer radius of the lithium lens. Also shown is the distribution of $\bar{p}$ accepted within 20π mm-mrad. Figure 12 shows the yield of $\bar{p}$ (primaries only) as a function of distance along the beam direction of the point of production. In addition to production within the target, $\bar{p}$ originating in the lithium lens and beryllium entrance window are observed. The distribution

of $\bar{p}$ accepted within 20π mm-mrad shows the depth-of-focus effect of the lens at the target and eliminates all $\bar{p}$ from the lens region. The center of the distribution is a few millimeters downstream from the center of the target, indicating a larger optimal distance to the lithium lens. The phase space distribution of all $\bar{p}$ at the downstream focal plane of the lens is shown in Figure 13. The only cut is that of the outer radius of the lithium lens. A clear band is seen for the production of $\bar{p}$ in the lithium lens region. The same distribution for an acceptance cut of 20π mm-mrad in both planes is shown in Figure 14. The change in the x' (= dx/dz) scale should be noted. The imposed elliptical cut is clearly seen and it is also obvious that the aspect ratio of the ellipse is not exactly at the optimum value.

4.2.1 Target Length

The expected yield of $\bar{p}$ is calculated as a function of target length, both for copper and tungsten targets. The results are presented in Figure 15 for two values of the transverse acceptance. Tungsten provides the higher yields and a choice of 5 to 6 cm for the target length is indicated.

Most of the accepted $\bar{p}$ originate from interactions by the primary proton beam. The fraction due to secondaries vs target length is shown for both copper and tungsten in Figure 16. Close to 22.0% of the $\bar{p}$ originate from secondaries at the

optimum tungsten target length. This fraction is essentially the same for 20 or 40π mm-mrad acceptances.

4.2.2 Proton Beam Size

The effect of beam size on the $\bar{p}$ yield is shown in Figure 17, for tungsten targets of several lengths and for two values of the acceptance. The yield increases almost linearly as the beam size is reduced down to rms sizes ($\sigma_x=\sigma_y$) of about 0.015 cm. For smaller beam sizes the yield starts to saturate, as multiple scattering begins to dominate the effective proton beam size.

As discussed in Section 4.1, the maximum number of protons per pulse that can be targeted is inversely proportional to the square of the beam size. Since the $\bar{p}$ yield only decreases linearly with increasing beam size, this will favor larger proton beam sizes if higher proton intensities can thereby be achieved. For the standard Fermilab parameters this effect is summarized in Table IV. The number of protons of 3×10^{12} per pulse is just below the present record Booster intensity.

4.2.3 Lithium Lens Parameters

The effect on $\bar{p}$ yield of increasing the gradient to 1500 T/m as a function of beam size appears also in Figure 17 for two values of the acceptance. For each gradient the distance between target and lens has been adjusted such that the center

of the target is at the upstream focal plane of the lens. For an acceptance of 20π mm-mrad the increase in gradient produces an increase of 10% in the yield for very small beam sizes. For 40π mm-mrad the $\bar{p}$ yield is clearly limited by a lens of 1000 T/m and 1 cm radius.

Figure 17 also shows that the effect of increasing the lens radius to 2 cm is identical to increasing the lens gradient.

It follows that the proposed lithium lens collector is well matched for the standard Fermilab parameters. If the acceptance of $\bar{p}$ is to be increased beyond 20π mm-mrad, either the gradient or the radius of the lens is to be increased to optimize their collection.

4.2.4 Lens Distance to Target

Figure 18 shows the $\bar{p}$ yield as a function of distance between the center of the target and the entrance to the lens for two values of the acceptance. The optimum occurs at a distance of 15 cm with at most a few percent increase in yield over the geometry with the center of the target at the upstream focal plane (14.45 cm).

4.2.5 Acceptance

In Figure 19 the $\bar{p}$ yield as a function of acceptance is shown. The yield is expressed as $\bar{p}$ per incident proton for a total longitudinal acceptance of $\Delta p/p=0.04$. The increase in yield, when reducing the proton beam rms size from 0.038 to 0.022 cm, is clearly seen below 20π mm-mrad. For larger emittances the present parameters of the collecting lens limit the yield for the smaller beam size.

The yield increases as the square of the acceptance up to 10π mm-mrad. The choice of $\Delta p/p$ of 0.04 and the acceptance of 20π mm-mrad is a compromise between number of $\bar{p}$ per pulse accepted, requirements of the cooling systems and the required aperture of the magnets in the first ring (Debuncher) of the Antiproton Source.

5. CERN

5.1 CERN Parameters

The $\bar{p}$ yields obtained for comparison with the measurements performed at the CERN Antiproton Accumulator are based on the geometry that includes a linear horn for collection. The horn geometry in CASIM is based on a numerical representation[22] of the inner surface and the assumption that the horn is of uniform thickness (0.07 cm) in a direction perpendicular to that surface. Multiple scattering within the material of the

horn is included. Acceptance cuts, assumed equal in both transverse planes, are performed with upright ellipses at the exit plane of the horn. The quoted yields are for the optimum aspect ratio of these ellipses for a given acceptance.

The geometry for the CERN calculations is shown in Figure 20, with the relevant parameters listed in Table V. For comparison with the horn geometry, yields for the target and lithium lens collection geometry of Figure 21 are included.

5.2 Results

Comparison of the predicted yields is performed with data obtained by the CERN Antiproton Accumulator staff during early operation. The yield measurements require $\bar{p}$ identification among all negative particles emerging from the target and that the longitudinal and transverse acceptances are known. This is achieved by storing the $\bar{p}$ into the accumulator ring until all pions have decayed. The longitudinal and transverse acceptances are thus determined within the ring. Hence, the yields are obtained through a procedure sensitive to the operation of the ring.

For the CERN geometry of Table V with a tungsten target, the calculated distribution of all $\bar{p}$ versus the angle at production is shown in Figure 22. The only cut is that of the outer radius of the horn. The distribution of these $\bar{p}$ within a 100π mm-mrad cut is also shown. The $\bar{p}$ yield as a function of

distance along the beam direction of the point of production is shown in Figure 23 along with the yield within a 100π cut. In addition to those originating from the target there are $\bar{p}$ created in the graphite windows. The phase space distribution of all $\bar{p}$ at the exit of the horn shown in Figure 24, has a "butterfly" shape more pronounced than in the Fermilab case. The $\bar{p}$ distribution is not upright but looks slightly convergent. The distribution of accepted $\bar{p}$ within the 100π mm-mrad cut is presented in Figure 25.

5.2.1 Target Length

The effect of target length on $\bar{p}$ yield is presented in Figure 26 both for copper and tungsten targets and for two values of the acceptance. A length of 11 cm optimizes the yield for tungsten at the 100π mm-mrad acceptance, while for smaller acceptance there is only minimal dependence on target length. For very long targets the yield of a copper target is predicted to exceed that of tungsten. It has been reported[23] that for targets of 11 cm in length copper yields are consistently larger by about 20% than those from heavier targets like lead. A possible resolution of this puzzle may reside in Equation (1). Figure 3 indicates that (if the data of Fermilab and of Dekkers et al. are ignored) the fit to the $\bar{p}$ production data may overestimate the cross section for lead by approximately 20% with respect to the data of Allaby et al. and

Eichten el al. A similar comparison with copper gives a more accurate representation of these last two sets of data. If it is assumed that the tungsten cross section is indeed overestimated by 20%, then it is predicted that the yield from copper equals that from tungsten for target lengths of about 9 cm. For 11 cm long targets the copper yield would then exceed that from tungsten by about 10%.

Included in Figure 26 is the effect of the target length for tungsten in the lithium lens geometry. A target length of 6 cm is indicated as in the Fermilab case. For both acceptances one expects to collect about 1.5 times the optimum number of $\bar{p}$ with the linear horn collector.

The calculated fraction of accepted $\bar{p}$ due to secondary interactions is shown in Figure 27.

5.2.2 Horn Current

Figure 28 compares CERN data[24] with calculations for the $\bar{p}$ yield from a 11 cm long, 0.60 cm diameter copper target, assuming a transverse acceptance in both planes of 85π mm-mrad. There is good agreement for the larger values of the horn current but the optimum yield occurs at significantly different values of the current. The calculated optimum yield is larger by a factor of 2. Although the distribution of $\bar{p}$ in transverse phase space at the horn exit for the nominal horn current of 146 kA is consistent with an upright ellipse, for a 170 kA

current there appears to be a converging $\bar{p}$ beam with an ellipse angle given by $\tan\xi = -0.48$ rad m^{-1}.

5.2.3 Acceptance

The calculated $\bar{p}$ yield as a function of the acceptance is presented in Figure 29. For the linear horn geometry both 11 cm long tungsten and copper targets are shown along with a 6 cm tungsten target and lithium lens geometry. Comparison is made with data available from the CERN Antiproton Accumulator staff.[25] For the larger of the measured yield curves there is good agreement for acceptances below 25π mm-mrad but the calculation predicts larger yields than are observed at the larger acceptances.

For comparison the design value for the CERN project[4] of 2.5×10^{-6} $\bar{p}$ per proton is also indicated. This value is close to the predictions for the lithium lens geometry.

6. Summary

Perhaps the most significant figure of merit of a $\bar{p}$ source is the rate at which $\bar{p}$ are accumulated. This relates directly to the average luminosity of the collider and hence to the event rates observed in experiments.

Table VI compares calculated results of the $\bar{p}$ collection rate for the Fermilab and CERN designs. The standard parameters are used with the choice of tungsten as target material in both cases. It can be observed in Table VI that the kinematical region and the lithium lens collection system of the Fermilab design offer substantial advantages. The larger proton intensity at CERN partially offsets these advantages.

The proton intensity in the Fermilab design is limited by the rotation of the proton bunches prior to targeting (to minimize the $\bar{p}$ longitudinal emittance) which precludes loading the Main Ring with more than a single Booster batch. Without this limitation the proton intensity could be increased by about a factor of seven although such a gain would impose presently unrealistic requirements on the $\bar{p}$ collection device and the stochastic cooling system.

Further improvements are possible both at Fermilab and at CERN. The MC program described above can be a valuable aid in studying the effects of many such improvement schemes in a quantitative way.

We thank the staff of the CERN Antiproton Accumulator and the Institute of Nuclear Physics, Novosibirsk, for many fruitful discussions. One of us, C.H., wishes also to thank these institutions for their warm hospitality.

References

1. G.I. Budker, Atomic Energy 22 (1967) 346; Sov. J. Atomic Energy 22 (1967) 438.
2. S. van der Meer, Report CERN/ISR-PO/72-31 (1972).
3. VAPP-NAP Group, A.N. Skrinsky 8th Int. Conf. H.E. Acc. Geneva (1971) 72. BNL, C. Baltay 6th Int. Conf. H.E. Acc. Stanford (1974) 572. D. Cline et al., Fermilab Report TM-687(1976). UNK-IHEP, T. Vsevolozskaja et al. INP-Novosibirsk 80-182 (1980) and Fermilab $\bar{p}$ note 185 (1981).
4. CERN, Design Study $p\bar{p}$ facility CERN/PS/AA 78-3.
5. See e.g., B.V. Chirikov et al., Nucl. Inst. Meth. 144 (1977) 129; F. Krienen and J. MacLachlan, IEEE NS-28 3 (1981) 2711.
6. A. Van Ginneken, Fermilab FN 272(1975).
7. C.W. Akerlof, Phys. Rev. D3 (1971) 645; J.V. Allaby et al., CERN Report 70-12 (1970); B. Alper et al., Nucl. Phys. B100 (1975) 237; J. Badier et al., Phys. Lett. 39B (1972) 414; L.M. Barkov et al., Serpukhov Report IHEP 79-92 (1979); W. Bozzoli, Nucl. Phys.. B140 (1978) 271; D. Dekkers et al., Phys. Rev. 137B (1965) 962; A.N. Diddens et al., Nuovo Cim. 31 (1964) 961; T. Eichten et al., Nucl. Phys. B44 (1972) 333; H.J. Frisch et al., Phys. Rev. Lett. 44 (1980) 511; K. Guettler et al., Nucl. Phys. B116 (1976) 77; P. Garbincius (Fermilab SAS group), private

communication; J.C. Sens, private communication, M.A.J. Botje, Thesis, Utrecht (1980); A.O. Vaisenberg et al., Zh. Eksp. Theor. Fiz. 29 (1979) 719.

8. D.C. Carey et al., Phys. Rev. Lett. 33 (1974) 327; D.C. Carey et al., Phys. Rev. D14 (1976) 1196; F.E. Taylor et al., Phys. Rev. D14 (1976) 1217; J.R. Johnson et al., Phys. Rev. D17 (1978) 1292.
9. See e.g., J. Hebert et al., Phys. Rev. D15 (1977) 1867.
10. S.J. Brodsky et al., Phys. Rev. Lett. 39 (1977) 1120.
11. L.M. Barkov et al., Serpukhov Report, IHEP 81-107 (1981).
12. R. Hagedorn and J. Ranft, Suppl. Nuovo Cim. 6 (1968) 169.
13. See e.g., J.G. Rushbrooke and B.R. Webber, Phys. Repts. 44 (1978) 1.
14. B. Rossi, High Energy Particles, Prentice Hall, N.J. (1952).
15. Fermilab Antiproton Source Design Report, Fermilab February 1982.
16. B.F. Bayanov et al., 10th Int. Conf. H.E. Acc., Protvino (1977) Vol. 2, p. 103.
17. T.A. Vsevolozskaya et al., Zh. Teor. Eksp. Fiz. 45 (1975) 2494; B.F. Bayanov et al., Zh. Teor. Eksp. Fiz. 48 (1978) 160; E.P. Colton, Fermilab $\bar{p}$ Note 120, March 1981.
18. B.F. Bayanov et al., Fermilab Report TM-1000, August 1980; B.F. Bayanov et al., Nuc. Inst. Meth. 190 (1981) 9; G.N. Silvestrov, Private Communication.

19. High Intensity Targeting Workshop, Univ. of Wisconsin Report, Fermilab April 1980.

20. F. Krienen and F. Mills, Fermilab $\bar{p}$ Note 70, May 1980; T. Vsevolozskaya et al., Fermilab Report TM-1048, 1981.

21. Sho Ohnuma, Fermilab Internal Report, unpublished.

22. S. van der Meer, Private Communication.

23. E. Jones et al., CERN Report PS/AA/ME/Note 10, February 1982.

24. R.P. Johnson, Private Communication.

25. H. Koziol, CERN Report PS/AA/ME/Note 4, December 1981.

Table I

Dependence of the Parameters of the Invariant Cross Section Formula on Incident Particle Type

	k	m
p,n	0.065	8.0
π^+	0.057	3.2
π^-	0.053	2.7

Table II

Dependence of the Parameters of the Invariant Cross Section Formula on Target Species

Target	a	b	c
H	1.00	0.00	0.00
Be	0.90	0.95	0.61
Al	1.22	1.15	0.87
Cu	1.50	1.43	1.56
W	1.69	1.38	1.79
Pb	1.73	1.37	1.83

Table III

Standard Fermilab Parameters

Proton Energy	120 GeV
Antiproton Energy	8.0 GeV
Antiproton Momentum	8.89 GeV/c
Proton Beam Size $\sigma_x=\sigma_y$(rms)	0.038 cm
Protons per Pulse	3.0×10^{12}
Cycle Time	2.0 sec.
Target Material	W or W-Rh
Target Length	5 to 7 cm
Target Diameter	> 0.20 cm
Li Lens Radius	1 cm
Li Lens Gradient	1000 T/m
Li Lens Length	15 cm
Li Lens Distance to Focal Plane	14.45 cm (f*)
Acceptance	20π mm-mrad
0° $\bar{p}$ Production $\frac{1}{\sigma}\frac{d\sigma}{d\Omega dp}$ [Eq.(1)]	$2.52\times10^{-1}\ \frac{\bar{p}}{\text{Ster. GeV/c}}$
Proton Collision Length	9.86 cm (Tungsten)
$\bar{p}$ Absorption Length	9.29 cm (Tungsten)

Table IV

Dependence of the Number of Antiprotons per Pulse into 20π mm-mrad Acceptance on Proton Beam Size

Proton Beam rms Size $\sigma_y=\sigma_y$(cm)	Maximum Protons per Pulse	$\bar{p}$ Yield (4% $\Delta p/p$)	$\bar{p}$ per Pulse
0.022	1.0×10^{12}	6.8×10^{-5}	0.68×10^{8}
0.031	2.0×10^{12}	5.7×10^{-5}	1.14×10^{8}
0.038	3.0×10^{12}	4.9×10^{-5}	1.46×10^{8}

Table V

Standard CERN Parameters

Proton Energy	26 GeV
Antiproton Energy	2.758 GeV
Antiproton Momentum	3.575 GeV/c
Proton Beam Size $\sigma_x=\sigma_y$(rms)	0.075 cm
Protons per Pulse	$> 1.0\times10^{13}$
Cycle Time	2.4 sec
Target Material	Rh or Cu
Target Length	11.0 cm
Target Diameter	0.3 cm
Horn Current	146 kA (Nominal)
Acceptance	100π mm-mrad
0° $\bar{p}$ Production $\frac{1}{\sigma}\frac{d\sigma}{d\Omega dp}$ [Eq.(1)]	$1.30\times10^{-2}\ \frac{\bar{p}}{\text{Ster. GeV/c}}$
Proton Collision Length	9.86 cm (Tungsten)
$\bar{p}$ Absorption Length	8.74 cm (Tungsten)

Table VI

Fermilab - CERN Comparison

	Fermilab	CERN	Ratio
$\bar{p}$ production <60mrad	2.19×10^{-3}	1.21×10^{-4}	17.4
$\bar{p}$ collected per proton	4.90×10^{-5}	1.42×10^{-6}	34.5
Max. no. of protons per second	1.50×10^{12}	5.00×10^{12}	0.30
$\bar{p}$ collected per second	7.35×10^{7}	7.10×10^{6}	10.4

Figure Captions

Figure 1: Invariant differential $\bar{p}$ production cross section vs incident proton momentum with p_t=0 and x=0 held constant. The solid line represents Eq. (1).

Figure 2: Invariant differential $\bar{p}$ production cross section vs x_R with p_t=0 held constant and $x \to \infty$. The solid line represents Eq. (1).

Figure 3: Invariant differential $\bar{p}$ production cross section vs p_t with x_R=0 held constant and $s \to \infty$. The solid line represents Eq. (1).

Figure 4: Differential $\bar{p}$ production cross sections on tungsten, in the laboratory in the forward direction $\bar{p}$ production from Eq. (1) (per interacting proton).

Figure 5: Total laboratory $\bar{p}$ production on tungsten below 30 mrad from Eq. (1) (per interacting proton).

Figure 6: Total laboratory $\bar{p}$ production on tungsten below 60 mrad from Eq. (1) (per interacting proton).

Figure 7: Total laboratory $\bar{p}$ production on tungsten below p_t=0.30 GeV/c from Eq. (1) (per interacting proton).

Figure 8: Total laboratory $\bar{p}$ production on tungsten below p_t=0.60 GeV/c from Eq. (1) (per interacting proton).

Figure 9: Maximum energy density, E_D, deposited by 120 GeV protons in a 5 cm tungsten target vs rms beam size. Number of protons on target, N_D, for a maximum energy density of 200 Jgm^{-1} vs rms proton beam size.

Figure 10: Standard Fermilab geometry for the target and $\bar{p}$ collection system.

Figure 11: Predicted $\bar{p}$ yield (unnormalized) vs production angle with respect to the (central) proton beam direction for all $\bar{p}$ emerging from the back face of the lithium lens and for those accepted within 20π mm-mrad.

Figure 12: Predicted yield of $\bar{p}$ due to primaries (unnormalized) as a function of distance along the beam direction for all $\bar{p}$ emerging from the back face of the lithium lens and for those accepted within 20π mm-mrad.

Figure 13: Predicted distribution of $\bar{p}$ in phase space (unnormalized) at the second focal plane of the lithium lens for all $\bar{p}$ emerging from the back face of the lithium lens.

Figure 14: Predicted distribution of $\bar{p}$ in phase space (unnormalized) at the second focal plane of the lithium lens and accepted within 20π mm-mrad.

Figure 15: Calculated yield of $\bar{p}$, per incident proton, as a function of target length.

Figure 16: Calculated fraction of $\bar{p}$ originating from secondary interactions.

Figure 17: Calculated yield of $\bar{p}$, per incident proton, as a function of proton beam rms beam size. The effect of increasing the lithium lens radius and magnetic field gradient are also shown.

Figure 18: Calculated variation of the $\bar{p}$ yield, per incident proton, as a function of distance between target center and entrance plane of the lithium lens.

Figure 19: Calculated $\bar{p}$ yield vs acceptance, within a longitudinal $\Delta p/p=0.04$.

Figure 20: Standard CERN Antiproton Accumulator geometry for the target and linear horn collection system.

Figure 21: A possible lithium lens collector geometry for the CERN Antiproton Accumulator.

Figure 22: Predicted $\bar{p}$ yield (unnormalized) vs production angle with respect to the (central) proton beam direction for all $\bar{p}$ transmitted through the horn and for those accepted within 100π mm-mrad.

Figure 23: Predicted yield of $\bar{p}$ due to primaries (unnormalized) as a function of distance along the beam direction for all $\bar{p}$ transmitted through the horn and for those accepted within 100π mm-mrad.

Figure 24: Predicted distribution in phase space at the horn exit for all $\bar{p}$ transmitted (unnormalized).

Figure 25: Predicted distribution in phase space at the horn exit within 100π mm-mrad (unnormalized).

Figure 26: Calculated yield of $\bar{p}$ as a function of target length for CERN horn and for lithium lens geometries.

Figure 27: Calculated fraction of $\bar{p}$ originating from secondary interactions for the CERN horn geometry.

Figure 28: Comparison of CERN data of $\bar{p}$ yield within $\Delta p/p=0.015$ as a function of horn current with calculations.

Figure 29: Comparison of experimental and calculated yield of $\bar{p}$ within $\Delta p/p=0.015$ vs acceptance for the CERN horn geometry. The predicted yield for the CERN lithium lens geometry is also shown.

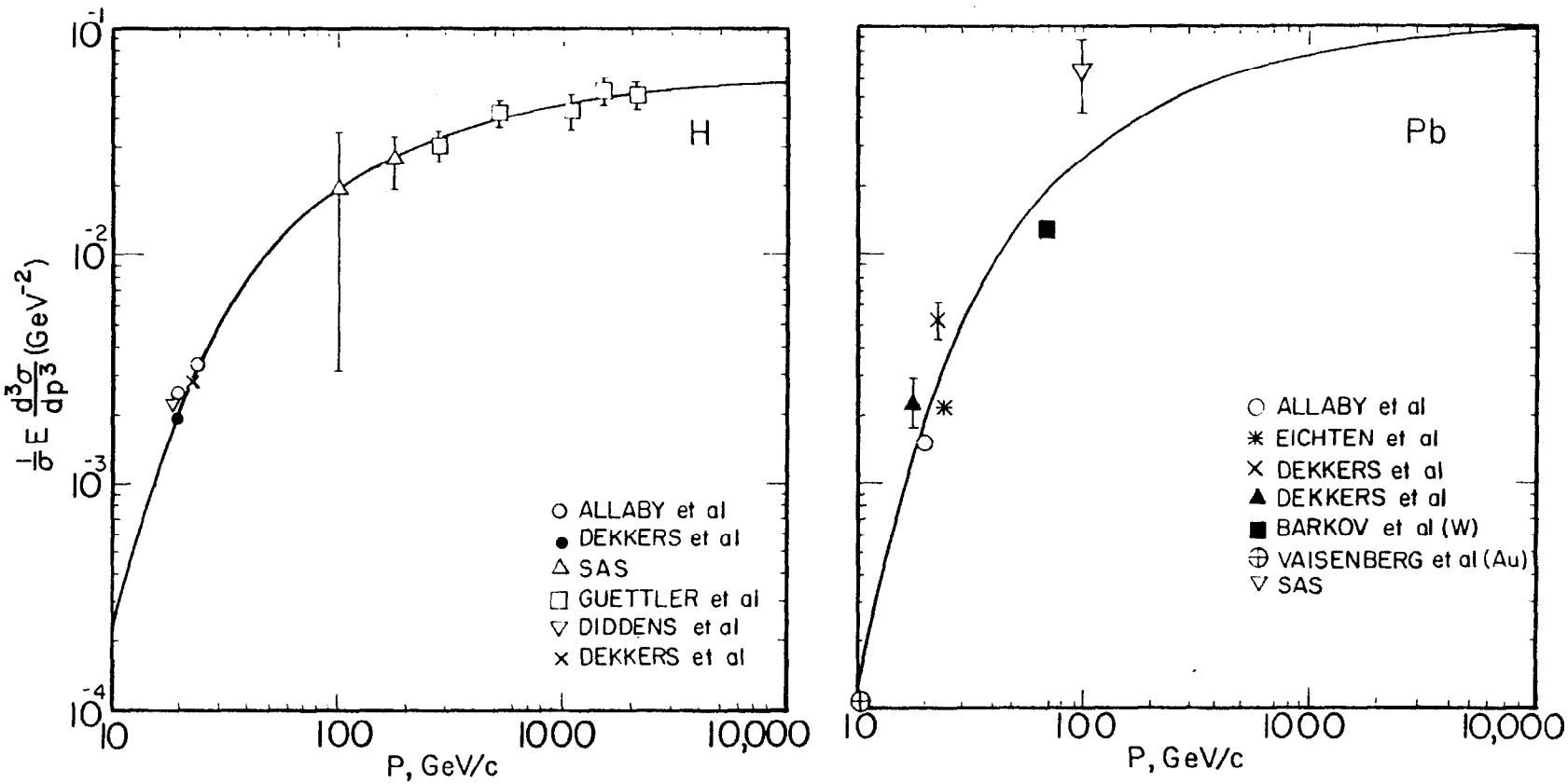
H
Pb
$\frac{1}{\sigma} E \frac{d^3\sigma}{dp^3}$ (GeV^{-2})
P, GeV/c
10
100
1000
10,000
10^{-1}
10^{-2}
10^{-3}
10^{-4}
○ ALLABY et al
● DEKKERS et al
△ SAS
□ GUETTLER et al
▽ DIDDENS et al
× DEKKERS et al
○ ALLABY et al
✳ EICHTEN et al
× DEKKERS et al
▲ DEKKERS et al
■ BARKOV et al (W)
⊕ VAISENBERG et al (Au)
▽ SAS

FIGURE 1

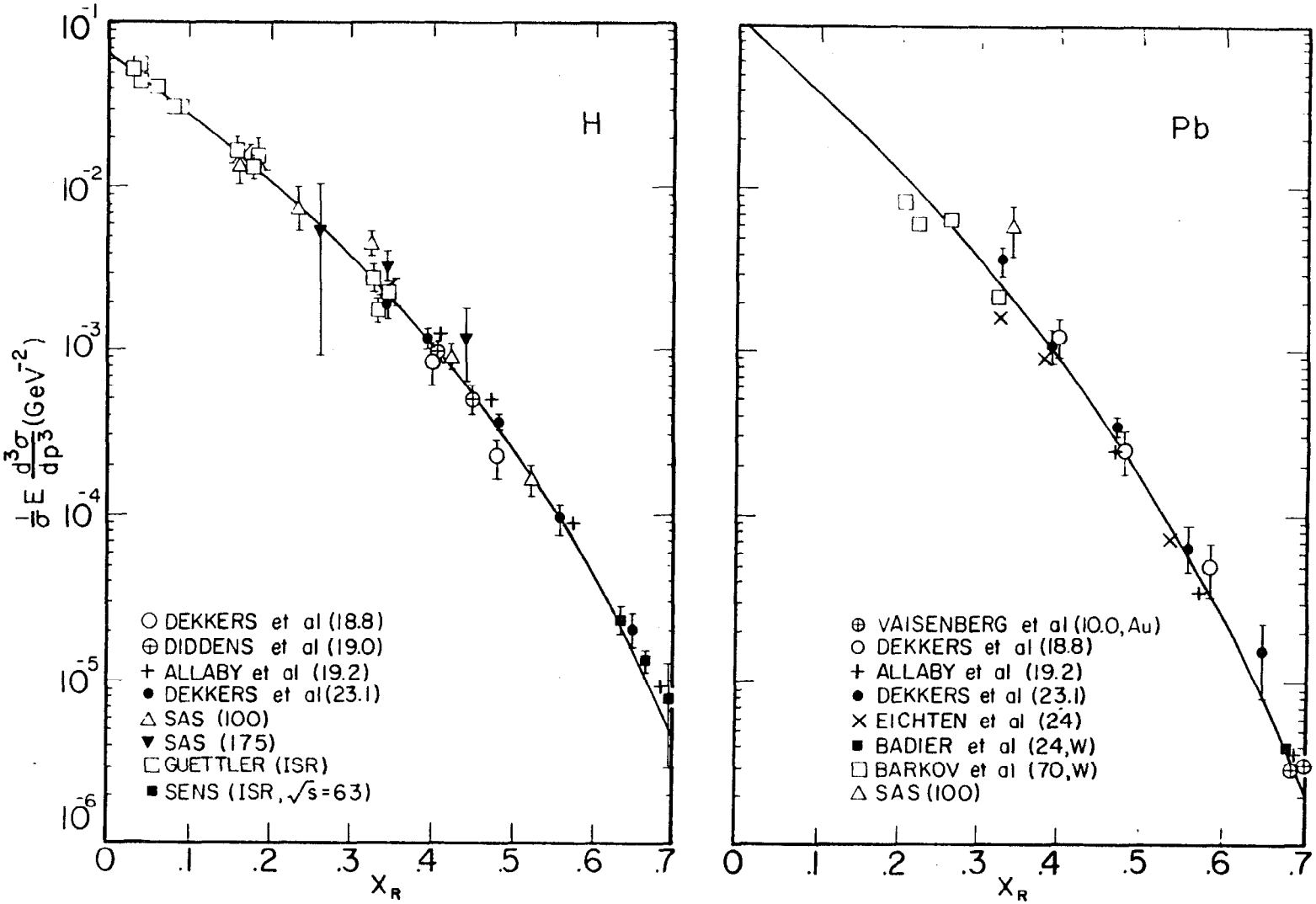
H
Pb
$\frac{1}{\sigma} E \frac{d^3\sigma}{dp^3} (GeV^{-2})$
X_R
O DEKKERS et al (18.8)
⊕ DIDDENS et al (19.0)
+ ALLABY et al (19.2)
• DEKKERS et al (23.1)
△ SAS (100)
▼ SAS (175)
□ GUETTLER (ISR)
■ SENS (ISR, $\sqrt{s}$=63)
⊕ VAISENBERG et al (10.0, Au)
O DEKKERS et al (18.8)
+ ALLABY et al (19.2)
• DEKKERS et al (23.1)
× EICHTEN et al (24)
■ BADIER et al (24, W)
□ BARKOV et al (70, W)
△ SAS (100)

FIGURE 2

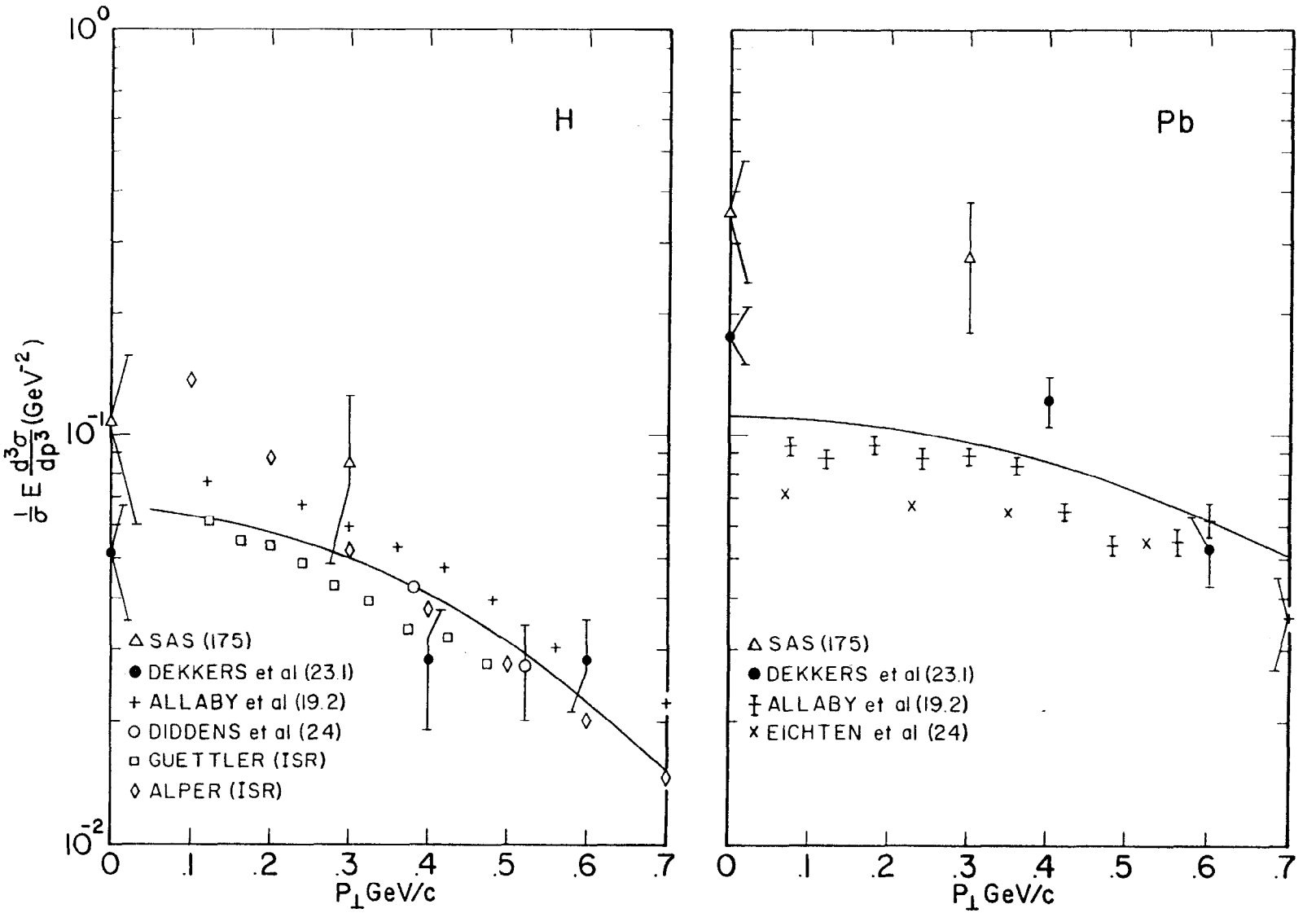
H
Pb
$\frac{1}{\sigma} E \frac{d^3\sigma}{dp^3} (GeV^{-2})$
10^0
10^{-1}
10^{-2}
0 .1 .2 .3 .4 .5 .6 .7
$P_\perp$ GeV/c
△ SAS (175)
● DEKKERS et al (23.1)
+ ALLABY et al (19.2)
○ DIDDENS et al (24)
□ GUETTLER (ISR)
◊ ALPER (ISR)
△ SAS (175)
● DEKKERS et al (23.1)
ǂ ALLABY et al (19.2)
× EICHTEN et al (24)

FIGURE 3

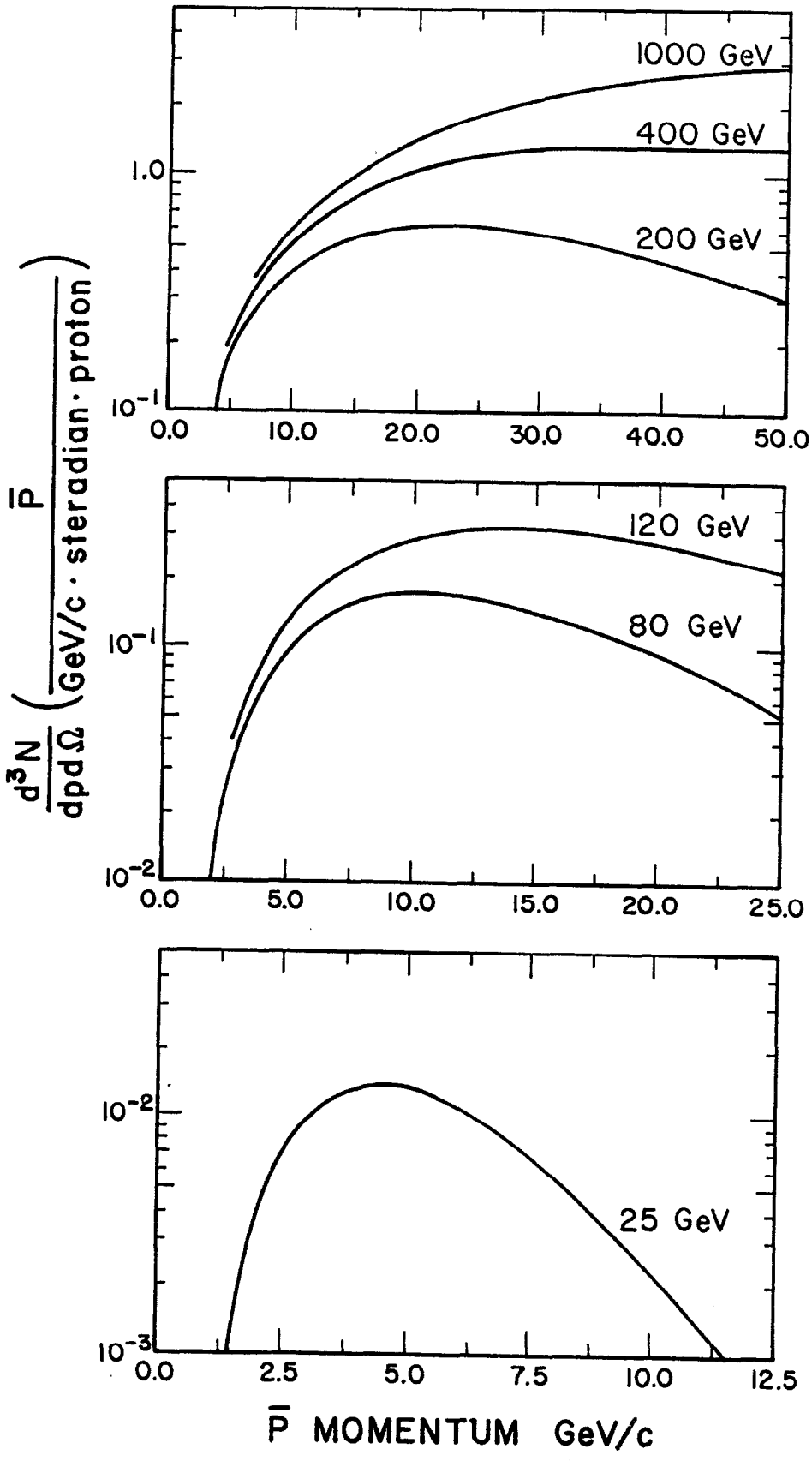
1000 GeV
400 GeV
200 GeV
120 GeV
80 GeV
25 GeV
1.0
10^{-1}
10^{-2}
10^{-3}
0.0
10.0
20.0
30.0
40.0
50.0
5.0
15.0
25.0
2.5
7.5
12.5
$\frac{d^3N}{dpd\Omega}\left(\frac{\bar{P}}{GeV/c \cdot steradian \cdot proton}\right)$
$\bar{P}$ MOMENTUM GeV/c

FIGURE 4

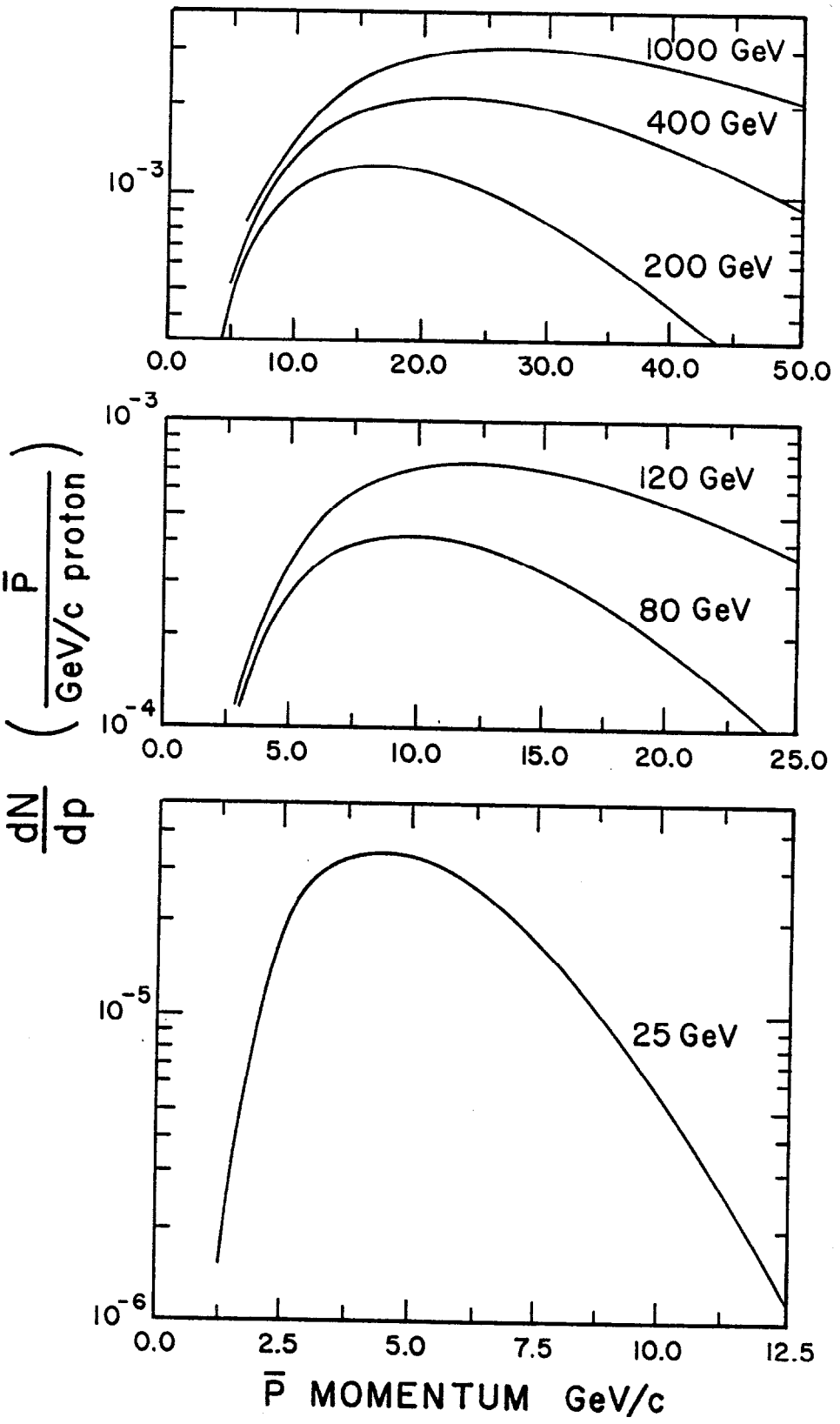
1000 GeV
400 GeV
200 GeV
120 GeV
80 GeV
25 GeV
10^{-3}
10^{-4}
10^{-5}
10^{-6}
0.0
10.0
20.0
30.0
40.0
50.0
5.0
15.0
25.0
2.5
7.5
12.5
$\frac{dN}{dp}$
$\left(\frac{\bar{p}}{\text{GeV/c proton}}\right)^{-1}$
$\bar{P}$ MOMENTUM GeV/c

FIGURE 5

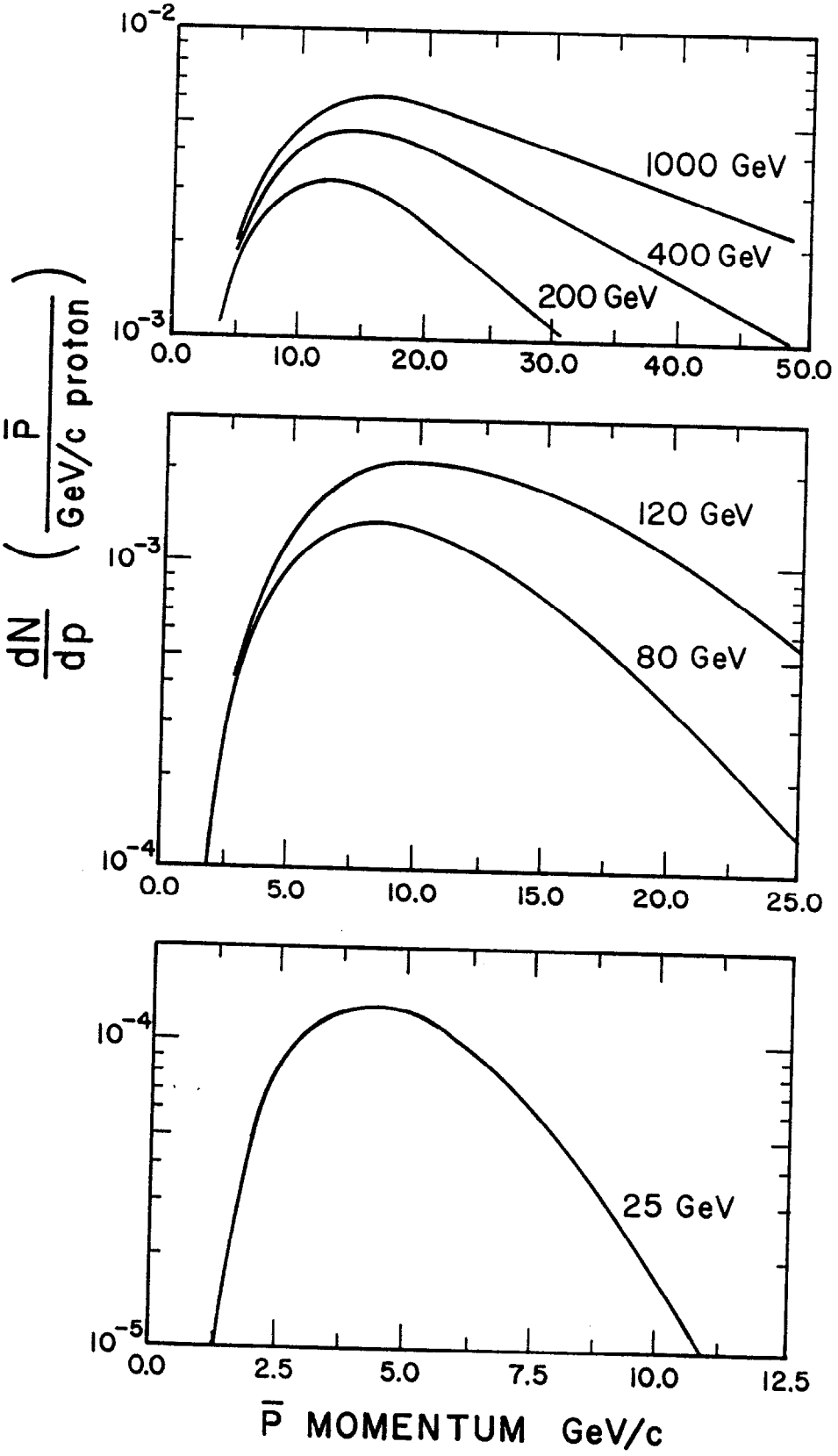
10^{-2}
10^{-3}
1000 GeV
400 GeV
200 GeV
0.0
10.0
20.0
30.0
40.0
50.0
$\frac{dN}{dp}$ ($\frac{1}{\text{GeV/c proton}}$)
10^{-3}
10^{-4}
120 GeV
80 GeV
0.0
5.0
10.0
15.0
20.0
25.0
10^{-4}
10^{-5}
25 GeV
0.0
2.5
5.0
7.5
10.0
12.5
$\bar{P}$ MOMENTUM GeV/c

FIGURE 6

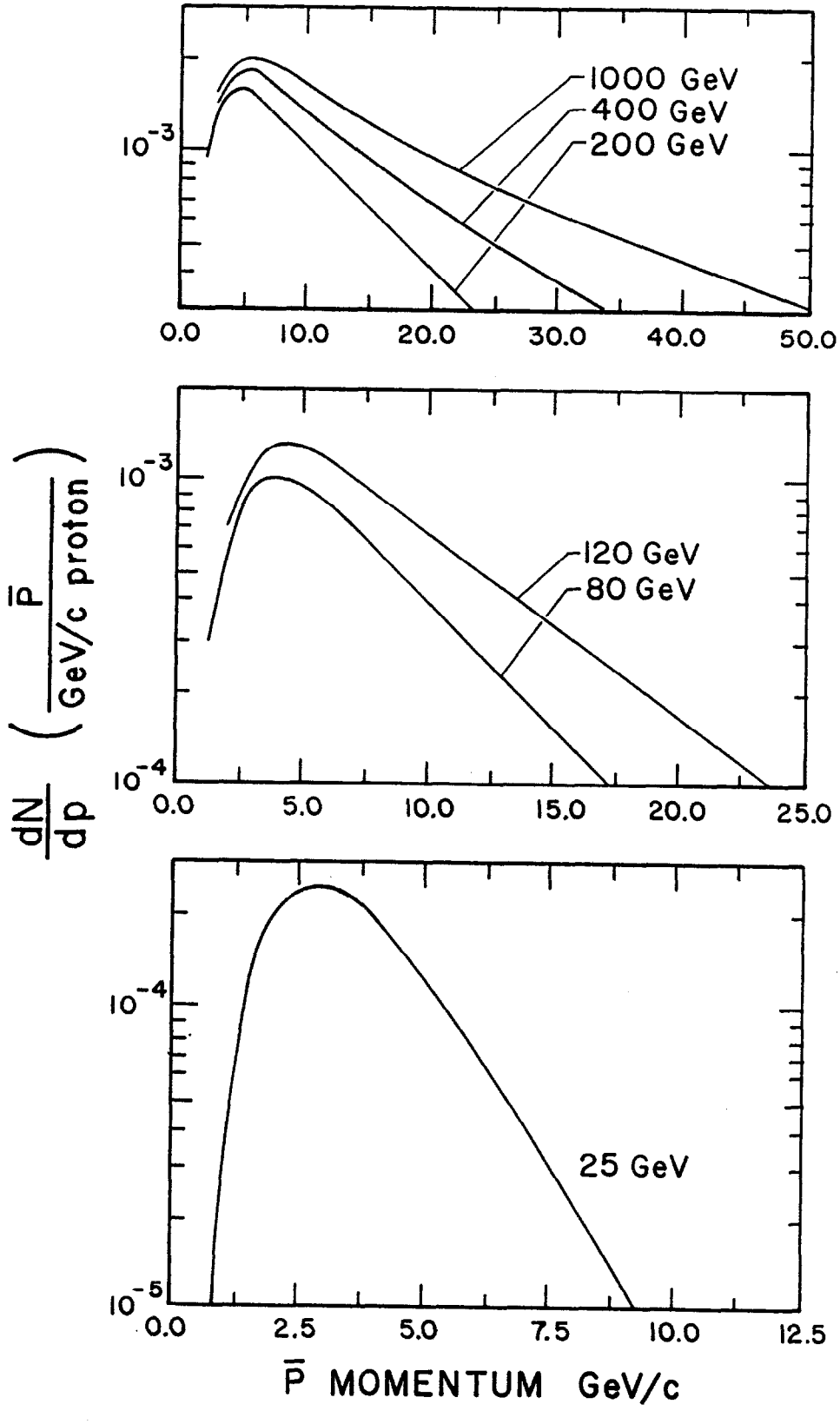
1000 GeV
400 GeV
200 GeV
120 GeV
80 GeV
25 GeV
10^{-3}
10^{-4}
10^{-5}
0.0
10.0
20.0
30.0
40.0
50.0
5.0
15.0
25.0
2.5
7.5
12.5
$\frac{dN}{dp}$ ($\frac{\bar{P}}{\text{GeV/c proton}}$)
$\bar{P}$ MOMENTUM GeV/c

FIGURE 7

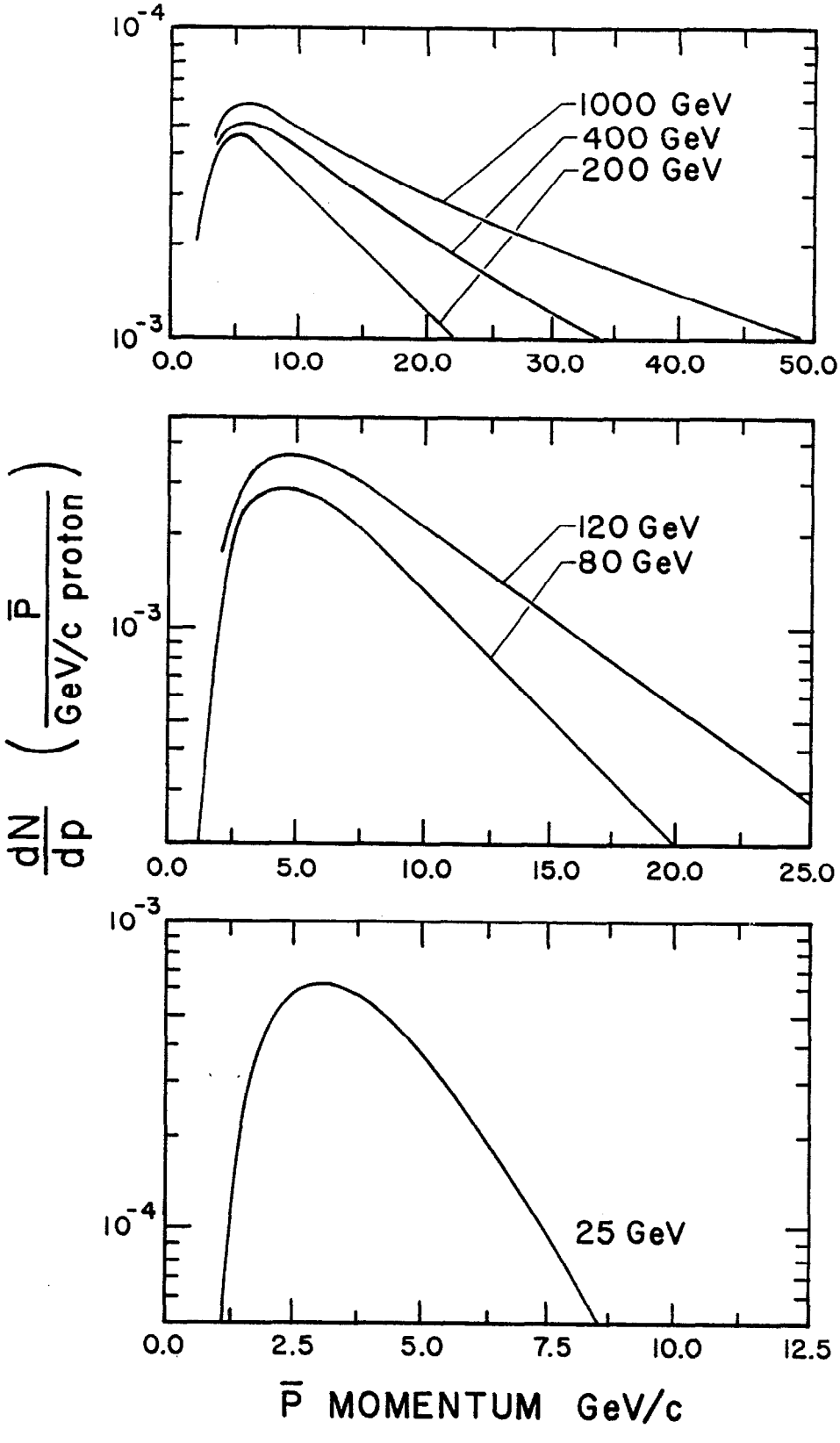
10^{-4}
1000 GeV
400 GeV
200 GeV
10^{-3}
0.0
10.0
20.0
30.0
40.0
50.0
10^{-3}
120 GeV
80 GeV
0.0
5.0
10.0
15.0
20.0
25.0
10^{-3}
10^{-4}
25 GeV
0.0
2.5
5.0
7.5
10.0
12.5
$\frac{dN}{dp}$ ($\frac{\bar{P}}{\text{GeV/c proton}}$)
$\bar{P}$ MOMENTUM GeV/c

FIGURE 8

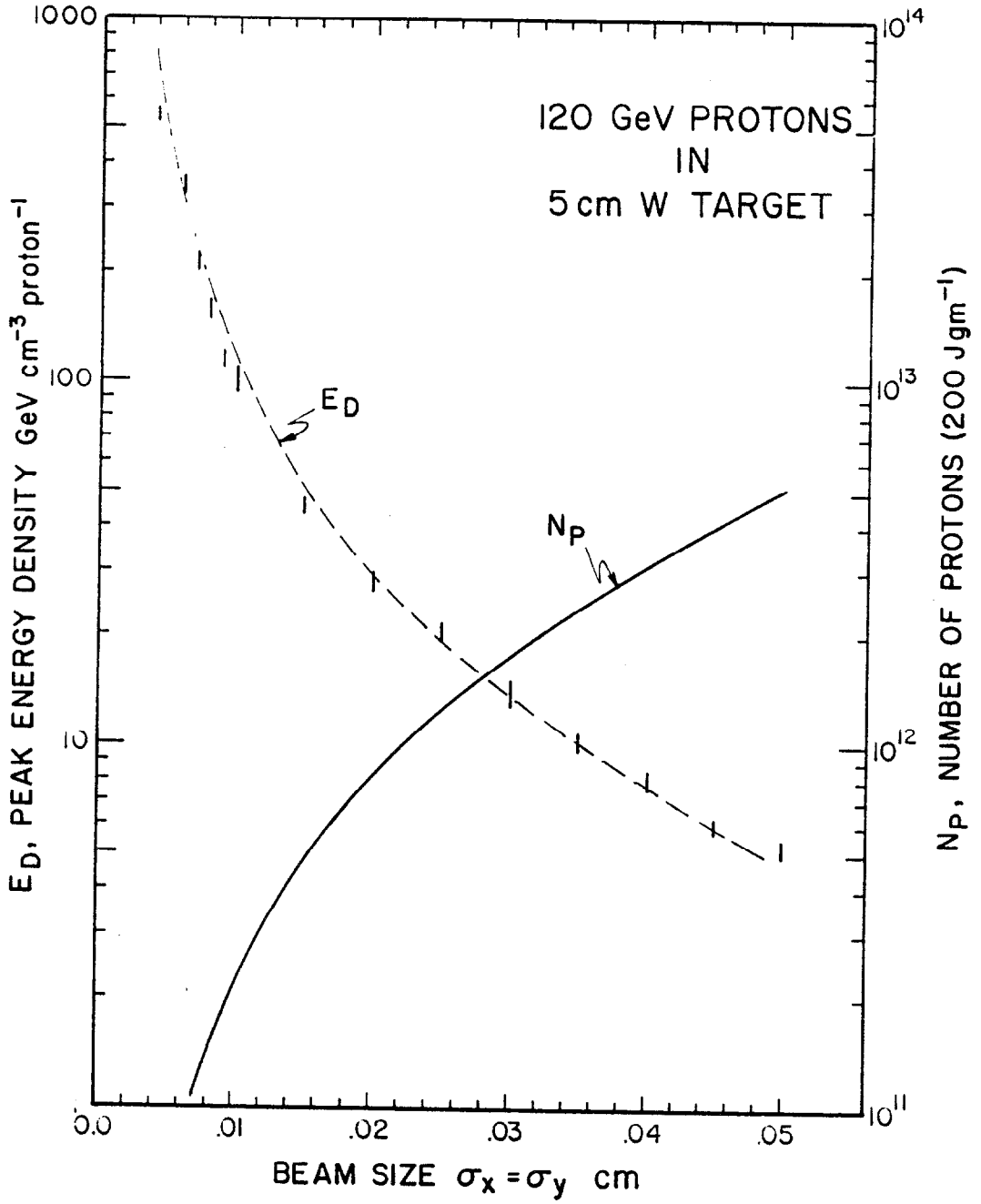
120 GeV PROTONS
IN
5 cm W TARGET
E_D
N_P
1000
100
10
1
10^{14}
10^{13}
10^{12}
10^{11}
0.0
.01
.02
.03
.04
.05
E_D, PEAK ENERGY DENSITY GeV cm^{-3} proton^{-1}
N_P, NUMBER OF PROTONS (200 J gm^{-1})
BEAM SIZE $\sigma_x = \sigma_y$ cm

FIGURE 9

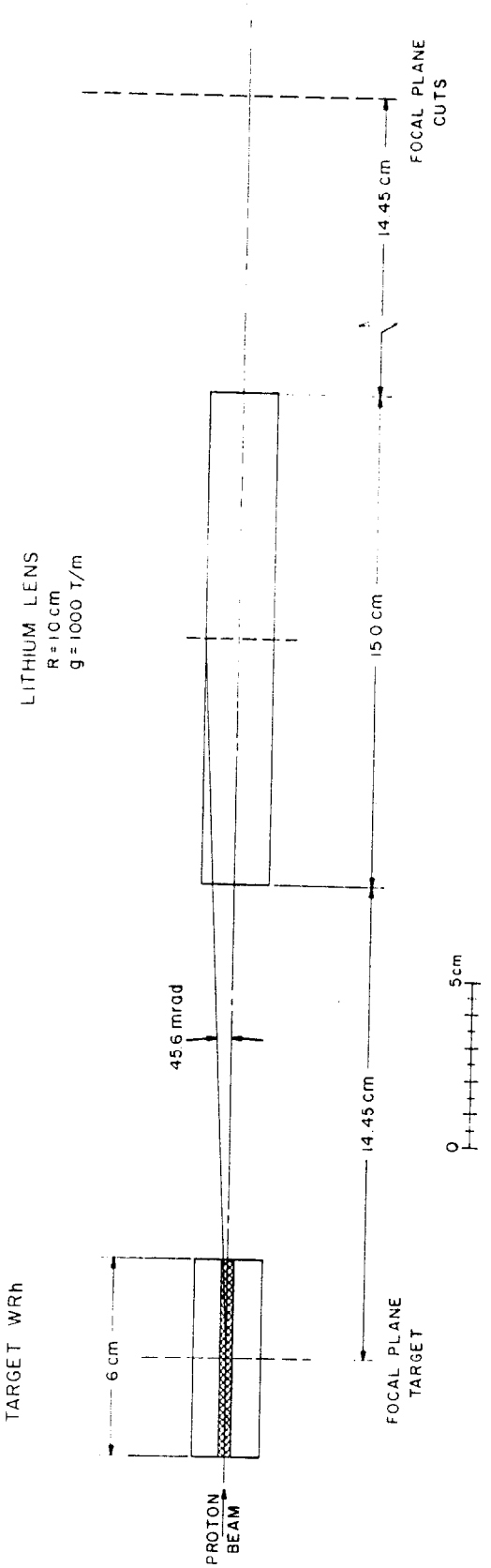
TARGET WRh
6 cm
PROTON BEAM
LITHIUM LENS
R = 1.0 cm
g = 1000 T/m
45.6 mrad
14.45 cm
FOCAL PLANE TARGET
15.0 cm
14.45 cm
FOCAL PLANE CUTS
0
5cm

FIGURE 10

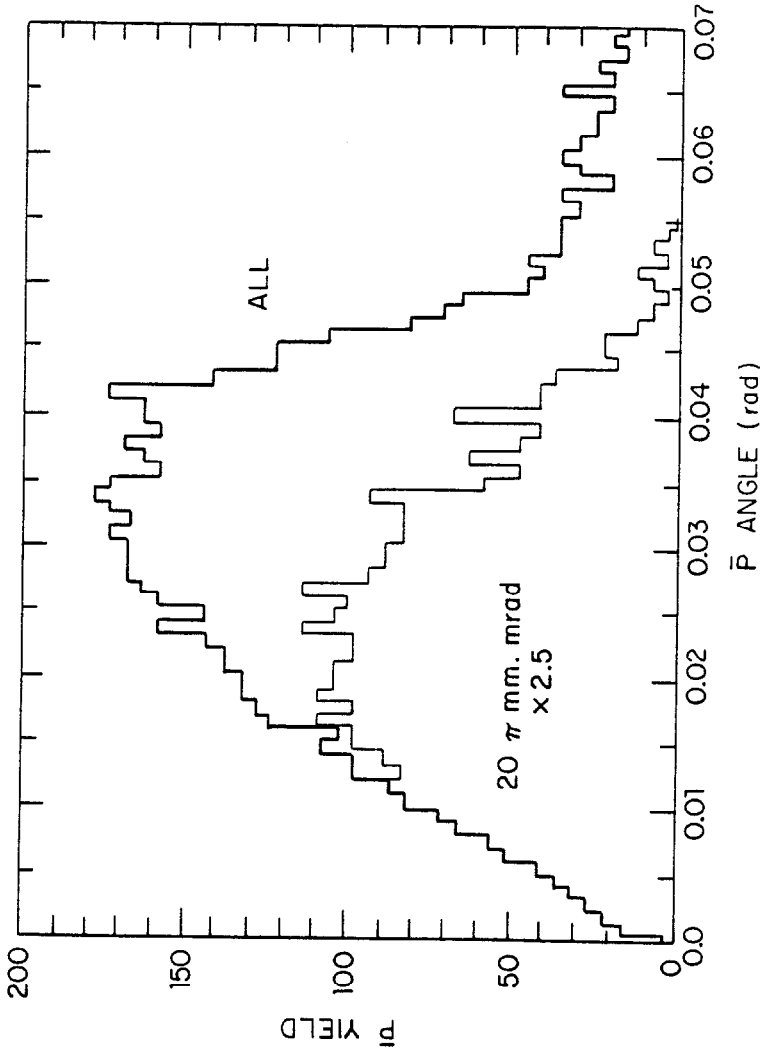
ALL
20 π mm. mrad
× 2.5
π YIELD
200
150
100
50
0
0.0
0.01
0.02
0.03
0.04
0.05
0.06
0.07
P̄ ANGLE (rad)

FIGURE 11

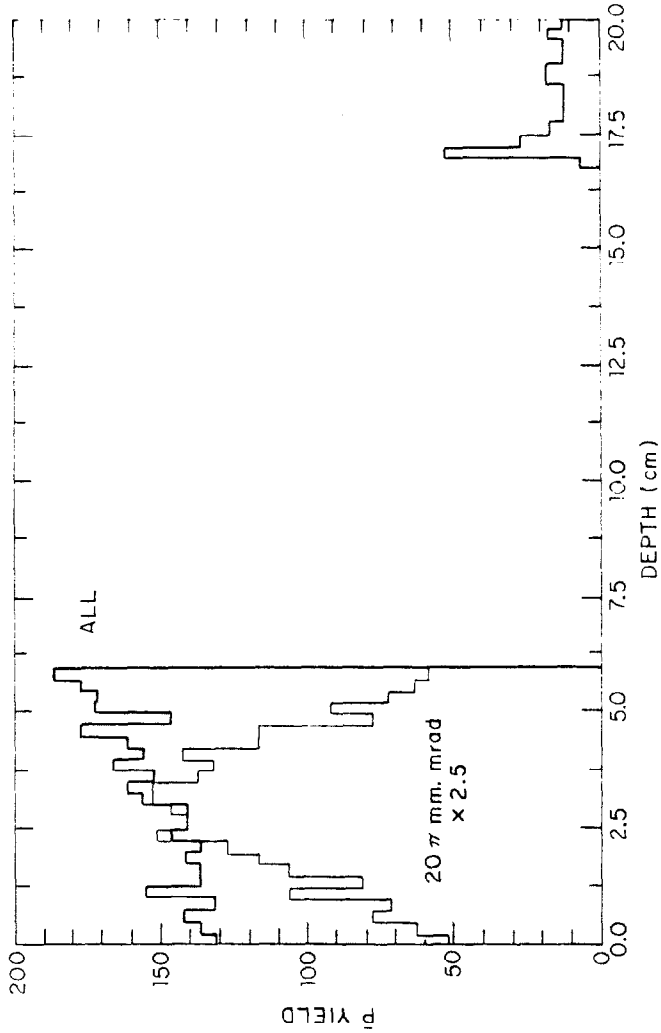
π YIELD
200
150
100
50
0
0.0
2.5
5.0
7.5
10.0
12.5
15.0
17.5
20.0
DEPTH (cm)
ALL
20 π mm. mrad
× 2.5

FIGURE 12

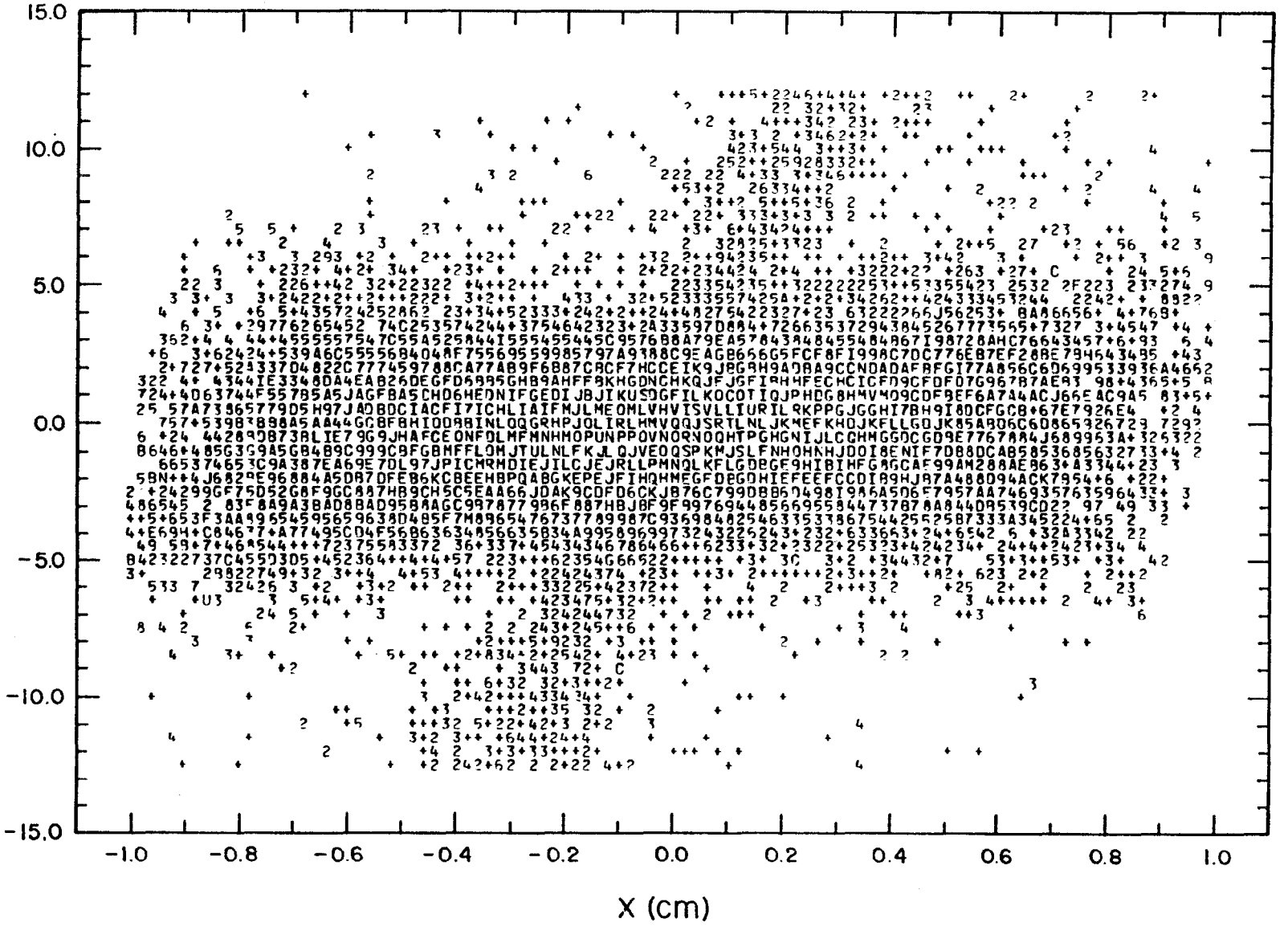

FIGURE 13

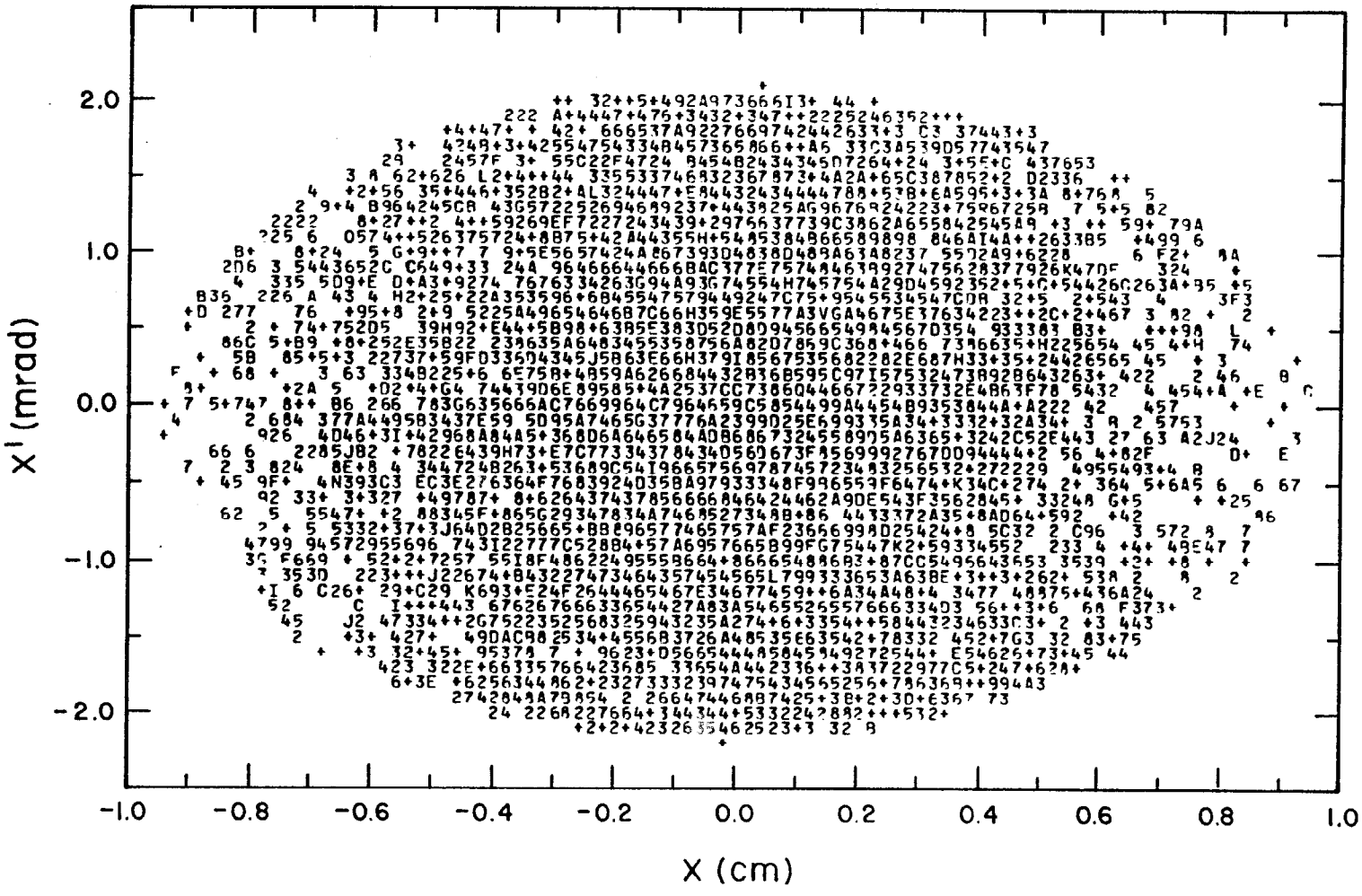

FIGURE 14

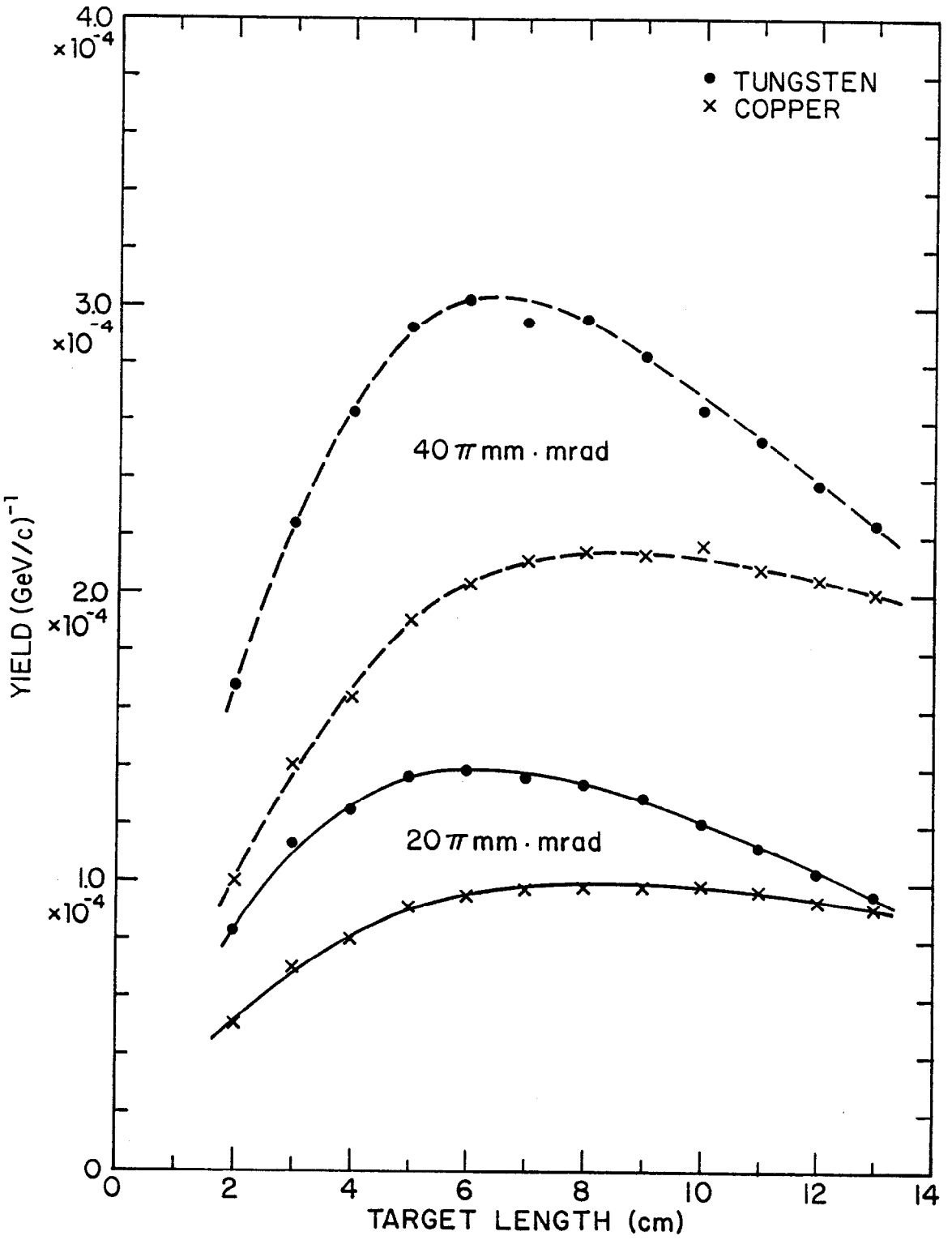
4.0
×10⁻⁴
3.0
×10⁻⁴
2.0
×10⁻⁴
1.0
×10⁻⁴
0
YIELD (GeV/c)⁻¹
• TUNGSTEN
× COPPER
40 π mm · mrad
20 π mm · mrad
0
2
4
6
8
10
12
14
TARGET LENGTH (cm)

FIGURE 15

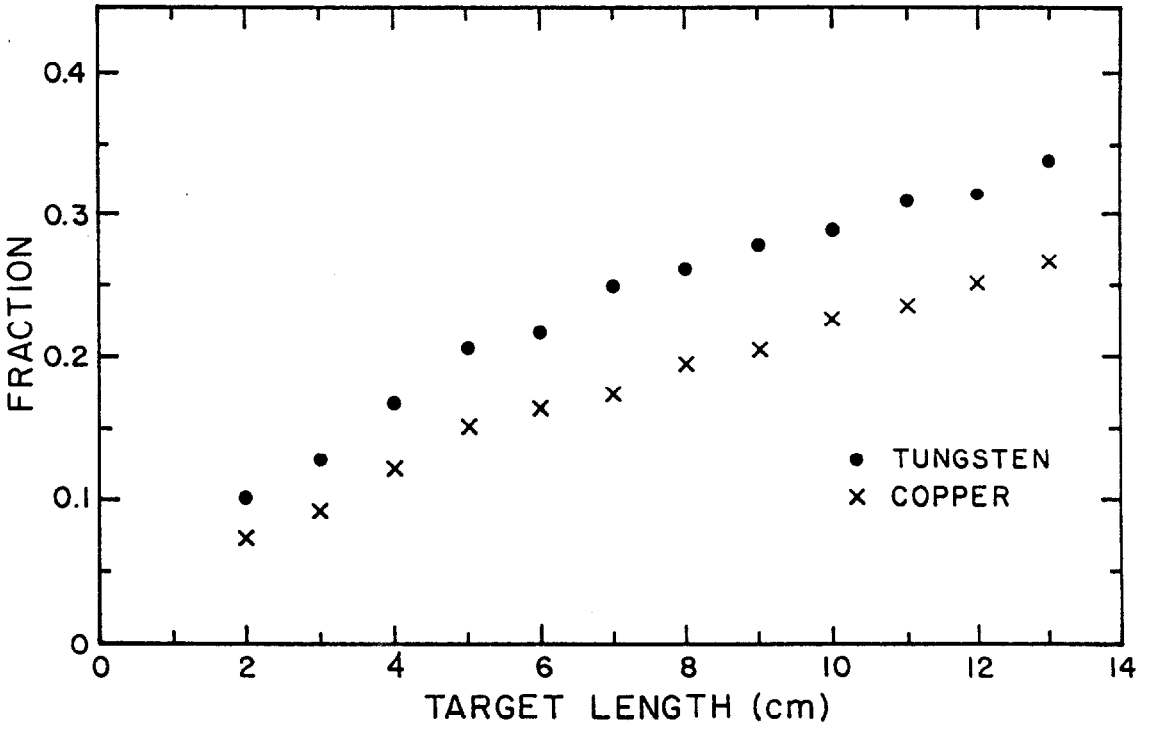
FRACTION
0.4
0.3
0.2
0.1
0
0
2
4
6
8
10
12
14
TARGET LENGTH (cm)
TUNGSTEN
COPPER

FIGURE 16

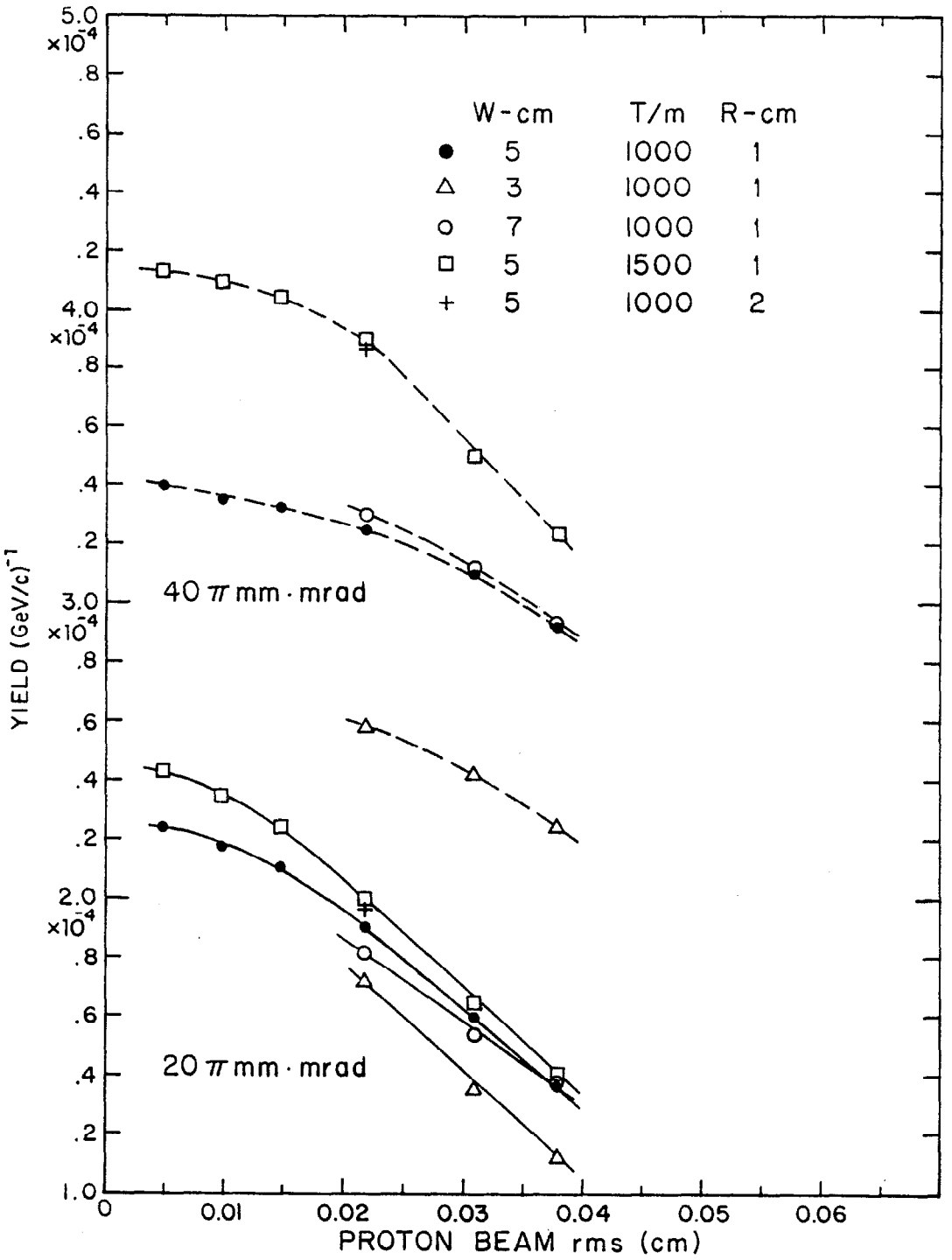
W-cm T/m R-cm
5 1000 1
3 1000 1
7 1000 1
5 1500 1
5 1000 2
40 π mm · mrad
20 π mm · mrad
YIELD (GeV/c)⁻¹
PROTON BEAM rms (cm)
5.0 ×10⁻⁴
4.0 ×10⁻⁴
3.0 ×10⁻⁴
2.0 ×10⁻⁴
1.0
0
0.01
0.02
0.03
0.04
0.05
0.06

FIGURE 17

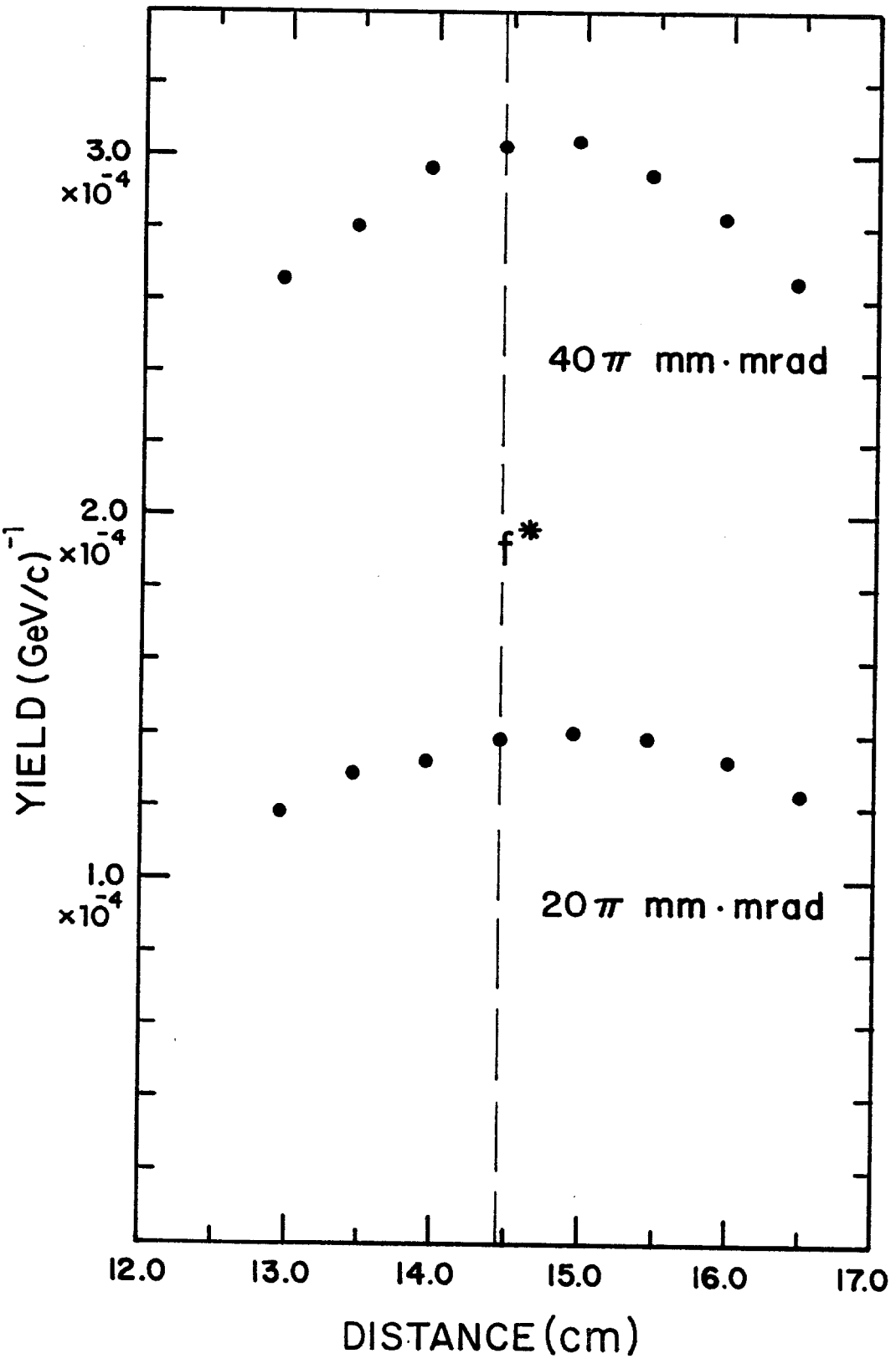
3.0
×10⁻⁴
2.0
×10⁻⁴
1.0
×10⁻⁴
YIELD (GeV/c)⁻¹
40π mm·mrad
20π mm·mrad
f*
12.0
13.0
14.0
15.0
16.0
17.0
DISTANCE (cm)

FIGURE 18

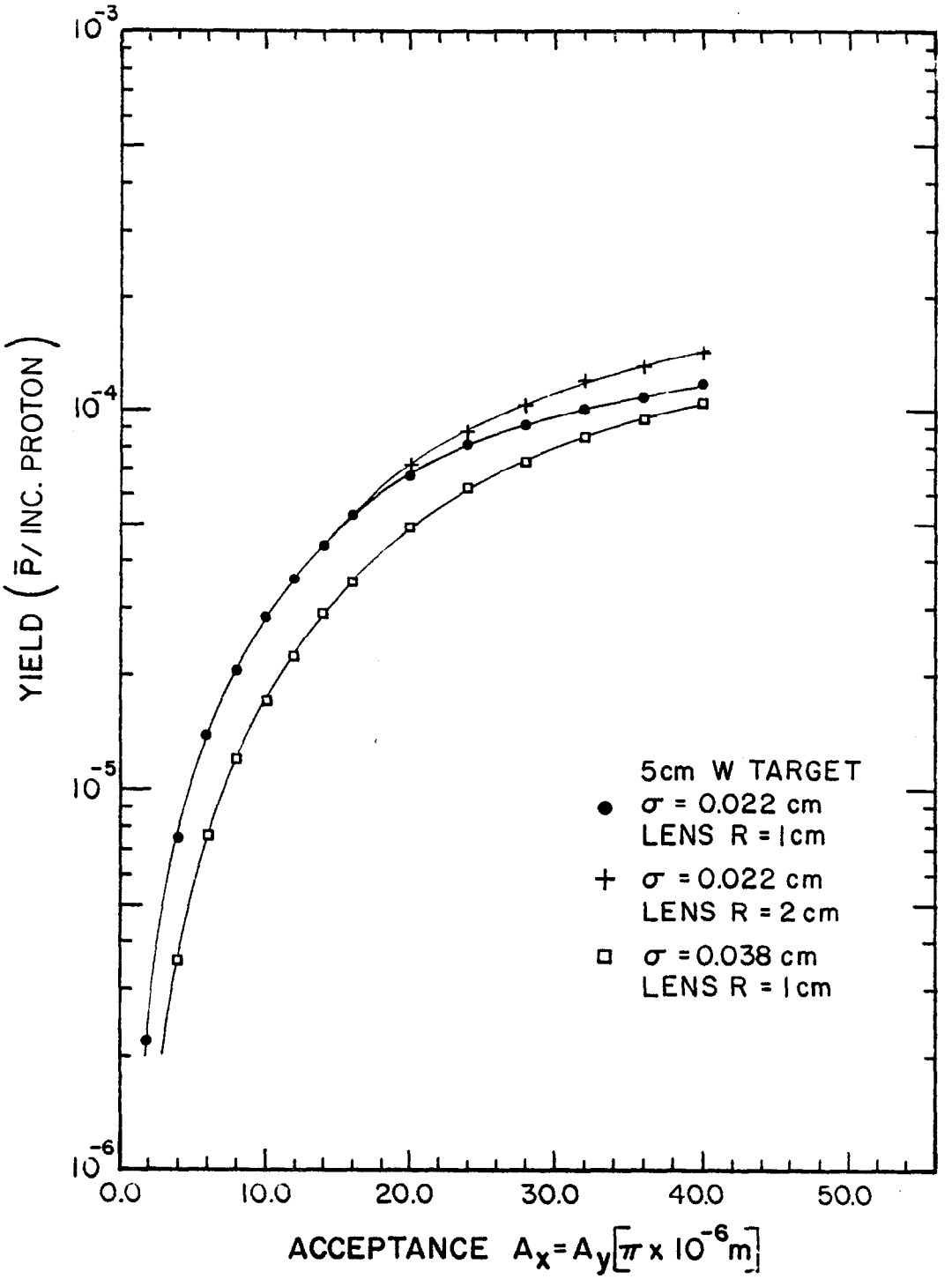
YIELD ($\bar{P}$/ INC. PROTON)
10^{-3}
10^{-4}
10^{-5}
10^{-6}
0.0
10.0
20.0
30.0
40.0
50.0
ACCEPTANCE $A_x = A_y[\pi \times 10^{-6} m]$
5cm W TARGET
● σ = 0.022 cm
LENS R = 1cm
+ σ = 0.022 cm
LENS R = 2 cm
□ σ = 0.038 cm
LENS R = 1cm

FIGURE 19

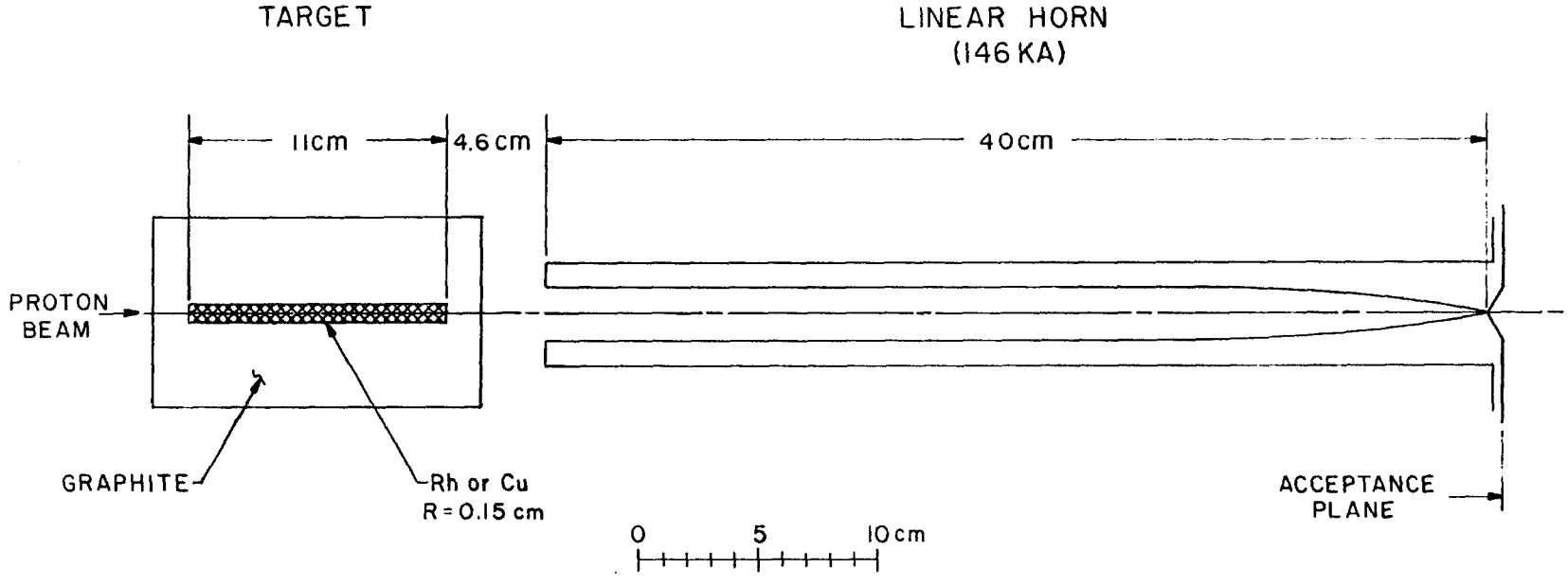
TARGET
LINEAR HORN
(146 KA)
11cm
4.6 cm
40cm
PROTON
BEAM
GRAPHITE
Rh or Cu
R = 0.15 cm
ACCEPTANCE
PLANE
0
5
10 cm

FIGURE 20

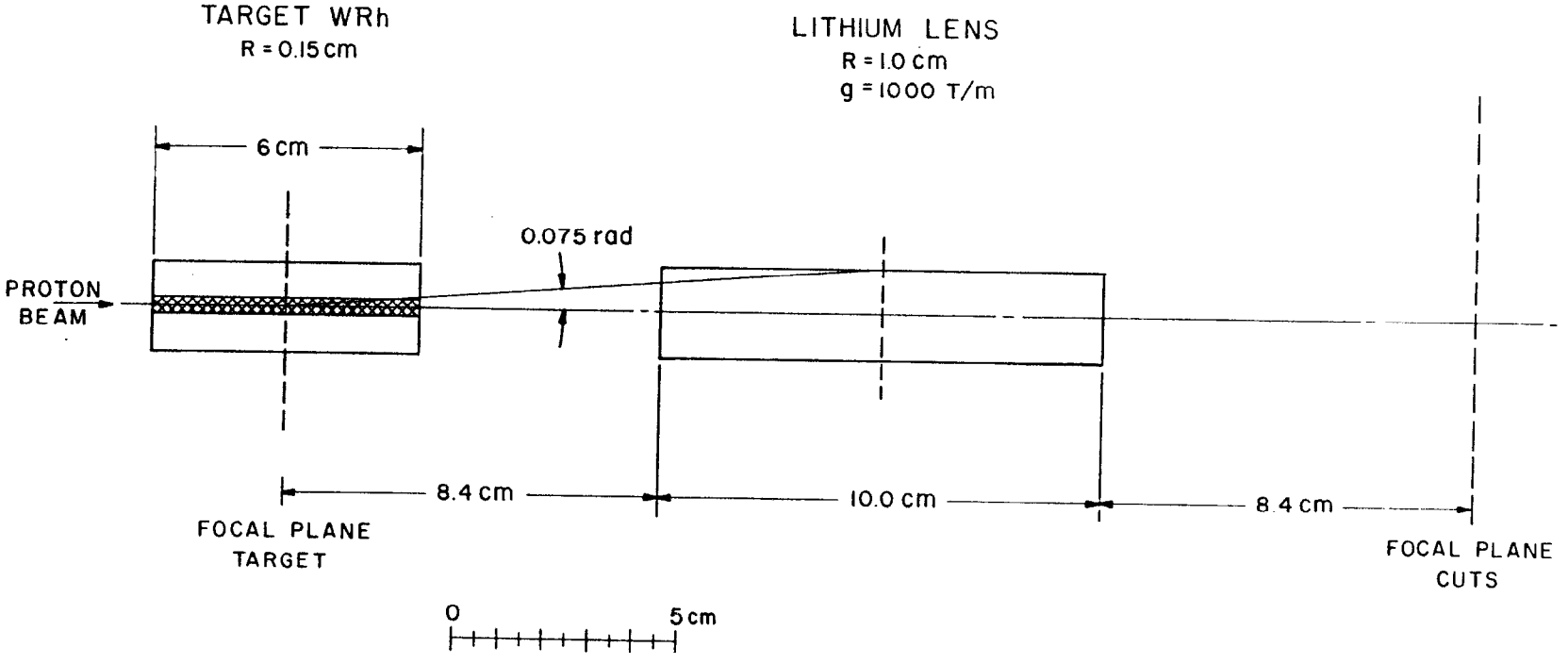
TARGET WRh
R = 0.15 cm
LITHIUM LENS
R = 1.0 cm
g = 1000 T/m
6 cm
0.075 rad
PROTON
BEAM
8.4 cm
10.0 cm
8.4 cm
FOCAL PLANE
TARGET
FOCAL PLANE
CUTS
0
5 cm

FIGURE 21

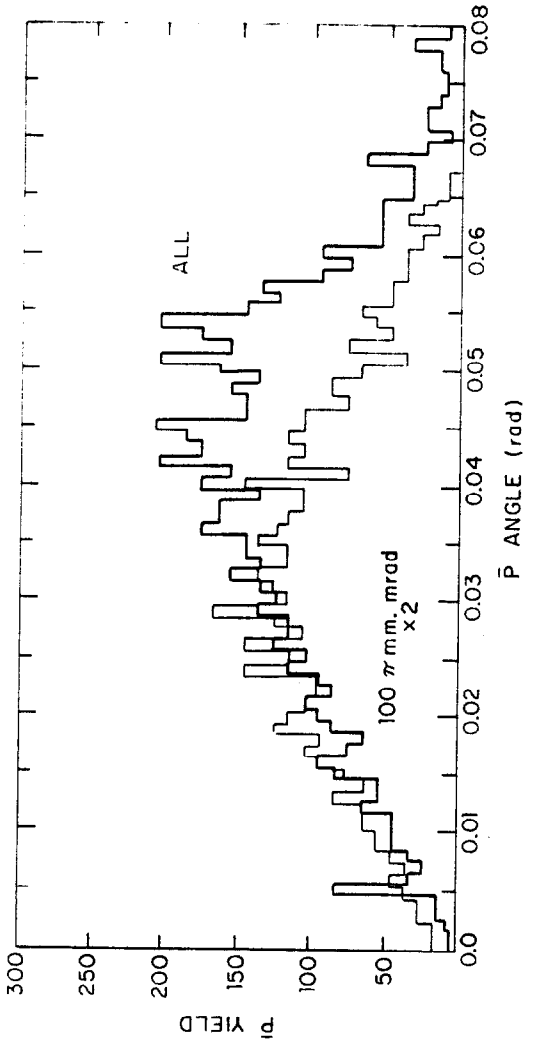
ALL
100 π mm. mrad
×2
π YIELD
P̄ ANGLE (rad)
0.0
0.01
0.02
0.03
0.04
0.05
0.06
0.07
0.08
50
100
150
200
250
300

FIGURE 22

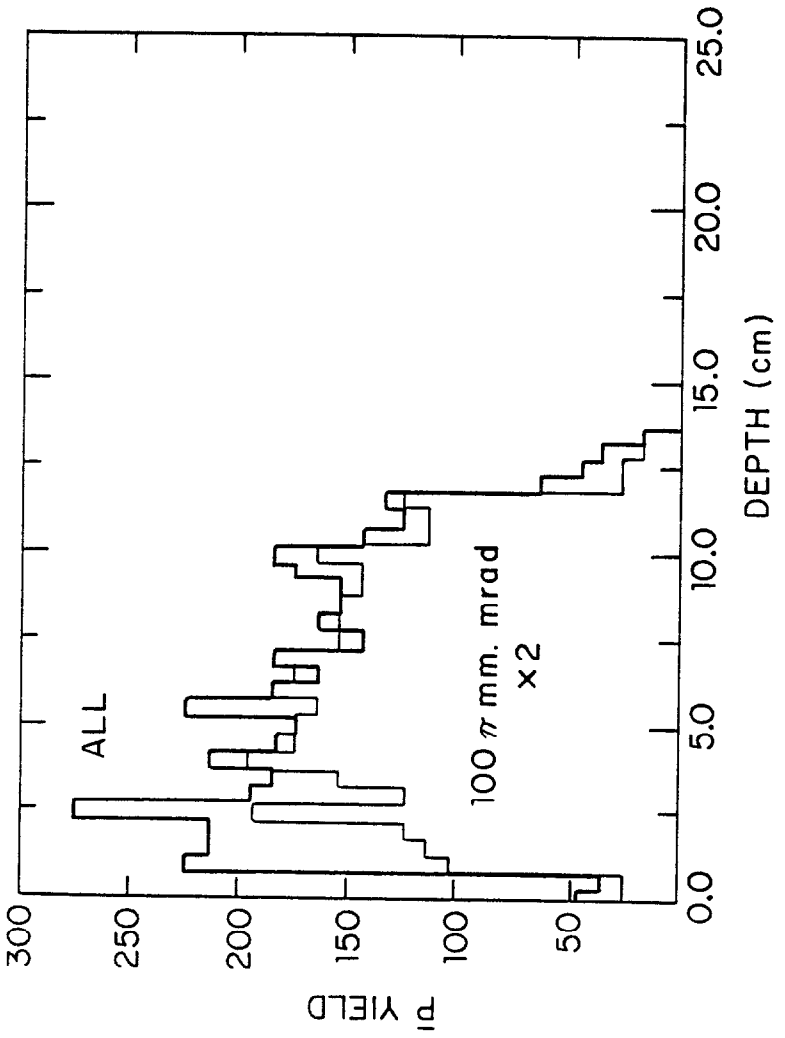
ALL
100 π mm. mrad
×2
DEPTH (cm)
0.0
5.0
10.0
15.0
20.0
25.0
π YIELD
50
100
150
200
250
300

FIGURE 23

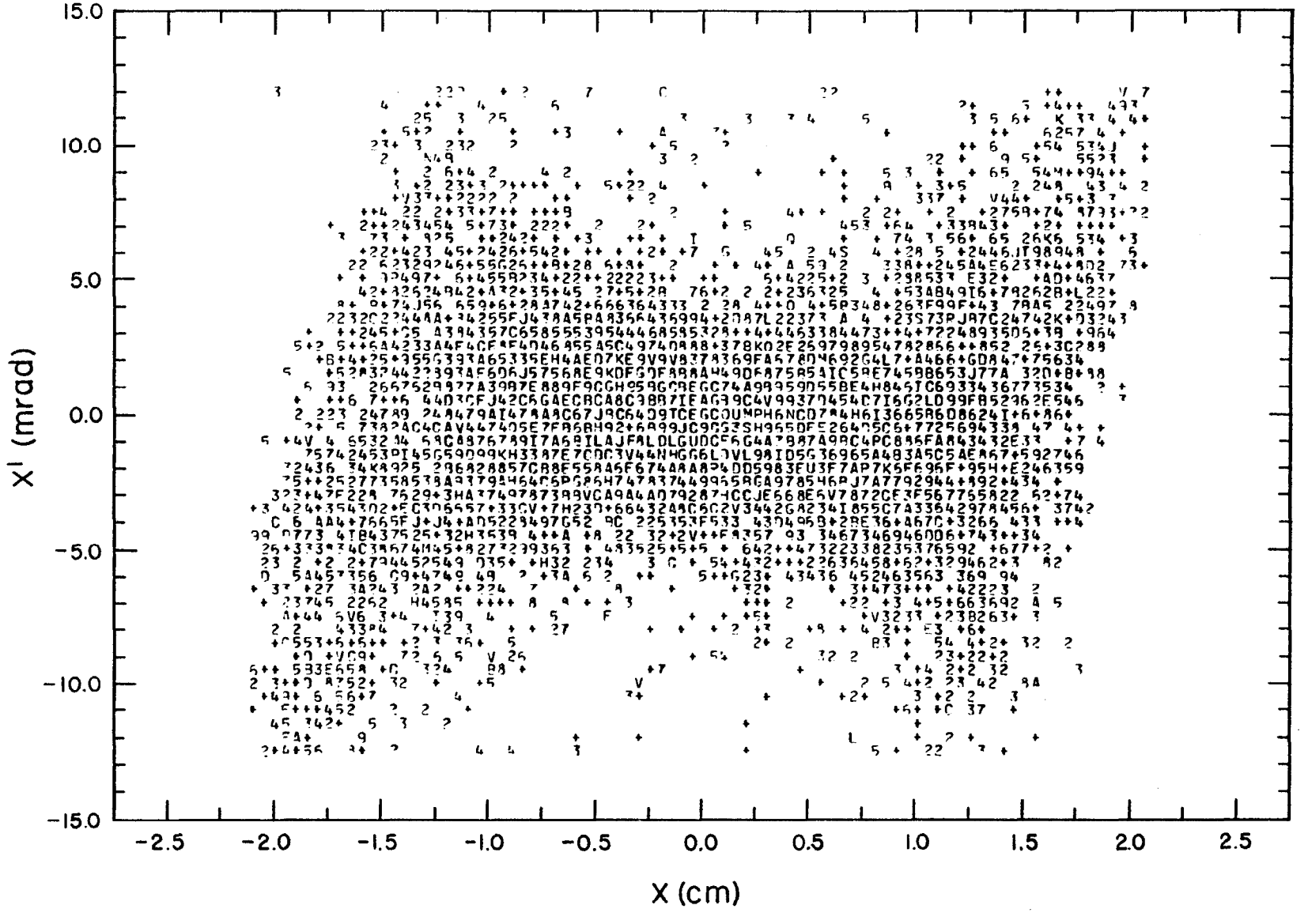

FIGURE 24

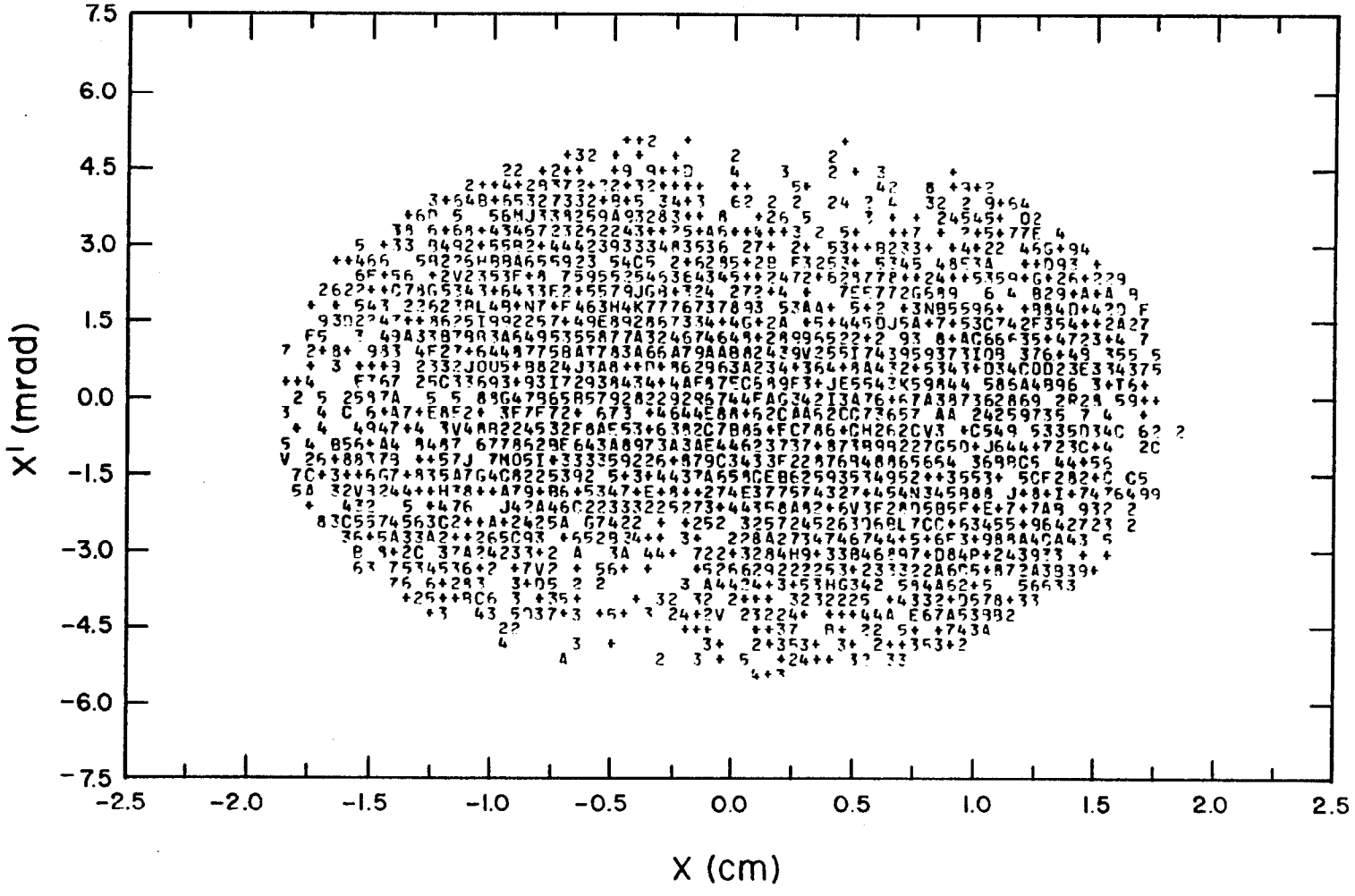
7.5
6.0
4.5
3.0
1.5
0.0
-1.5
-3.0
-4.5
-6.0
-7.5
X' (mrad)
-2.5
-2.0
-1.5
-1.0
-0.5
0.0
0.5
1.0
1.5
2.0
2.5
X (cm)

FIGURE 25

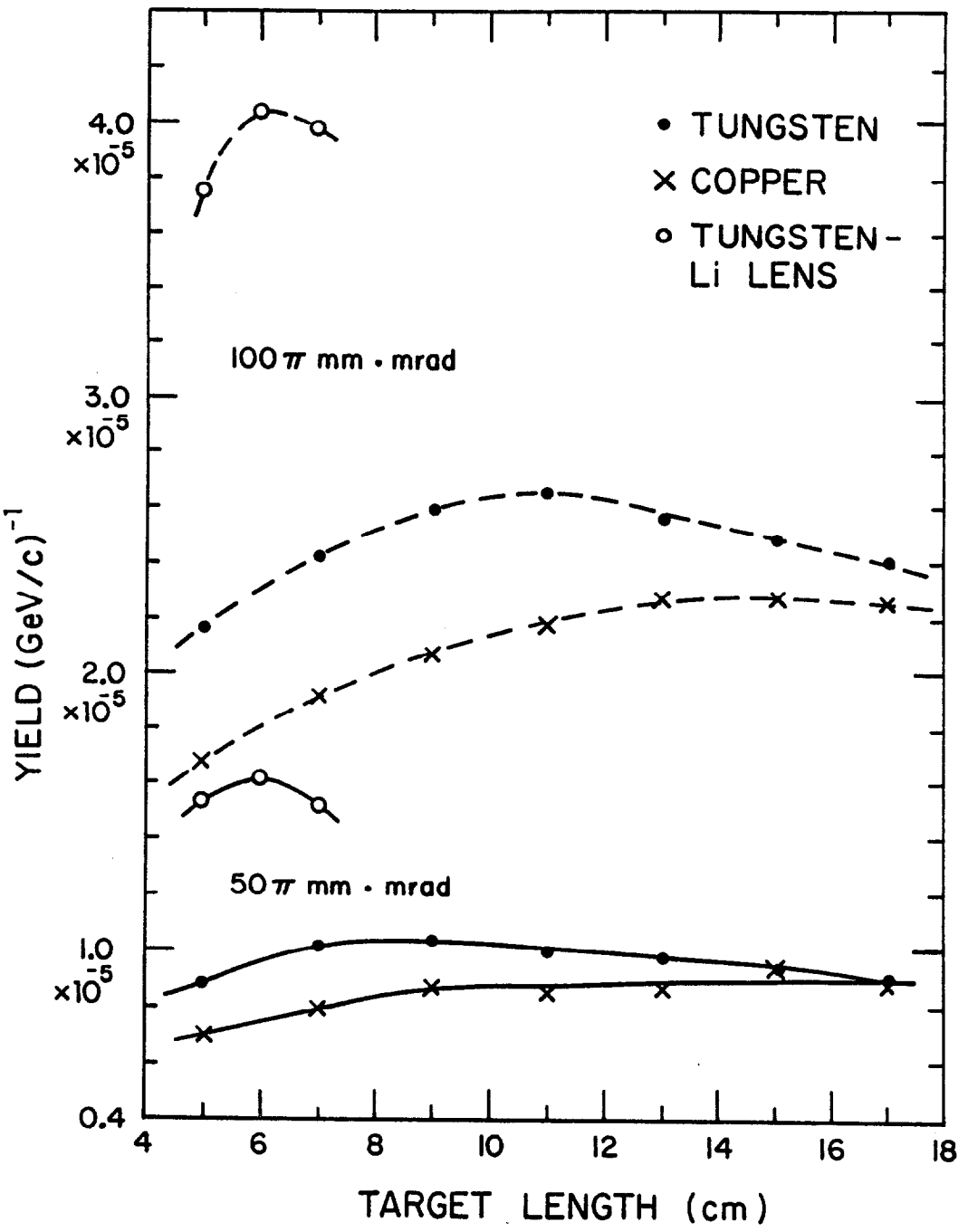
• TUNGSTEN
× COPPER
o TUNGSTEN-
Li LENS
100π mm • mrad
50π mm • mrad
YIELD (GeV/c)⁻¹
4.0 ×10⁻⁵
3.0 ×10⁻⁵
2.0 ×10⁻⁵
1.0 ×10⁻⁵
0.4
4
6
8
10
12
14
16
18
TARGET LENGTH (cm)

FIGURE 26

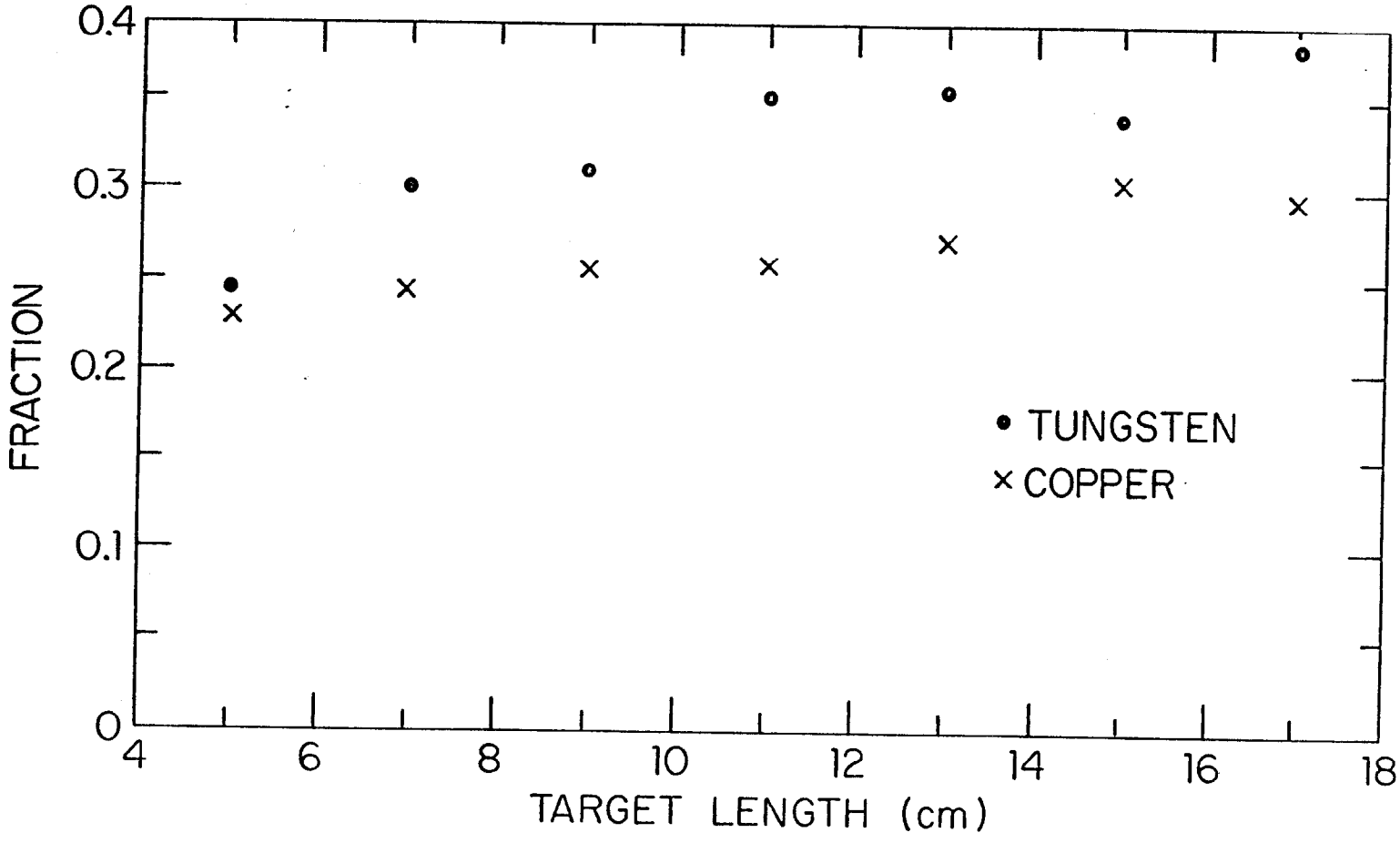
0.4
0.3
0.2
0.1
0
FRACTION
4
6
8
10
12
14
16
18
TARGET LENGTH (cm)
• TUNGSTEN
× COPPER

FIGURE 27

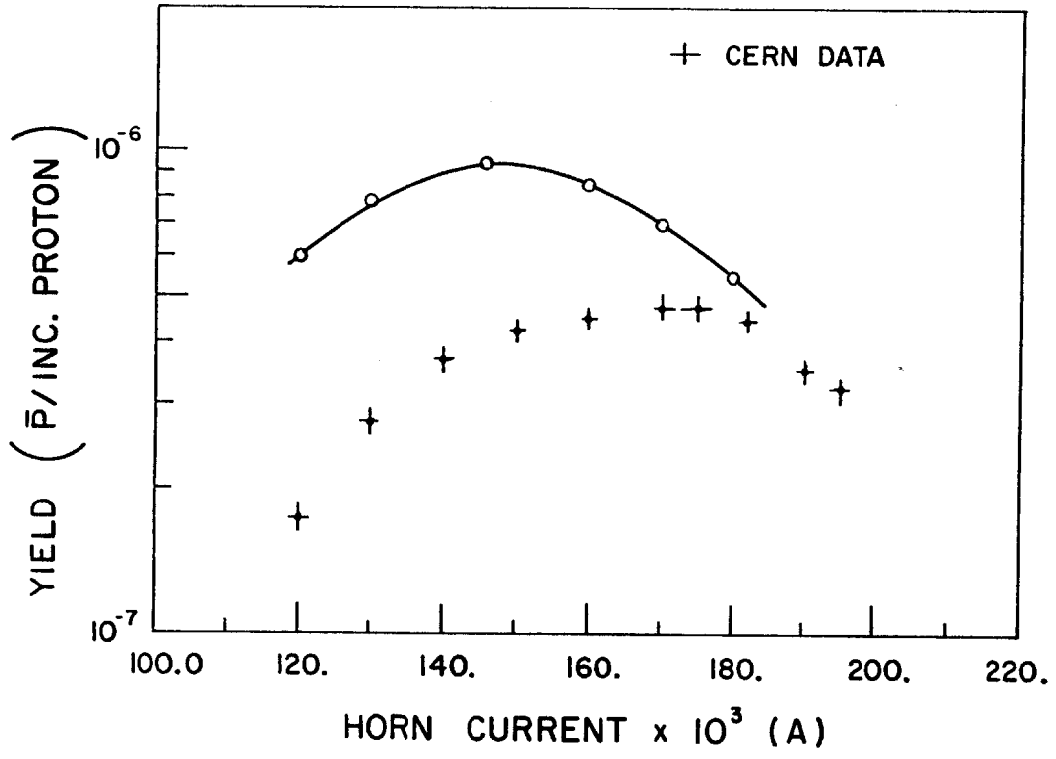
+ CERN DATA
YIELD ($\bar{P}$/INC. PROTON)
10^{-6}
10^{-7}
100.0
120.
140.
160.
180.
200.
220.
HORN CURRENT x 10^3 (A)

FIGURE 28

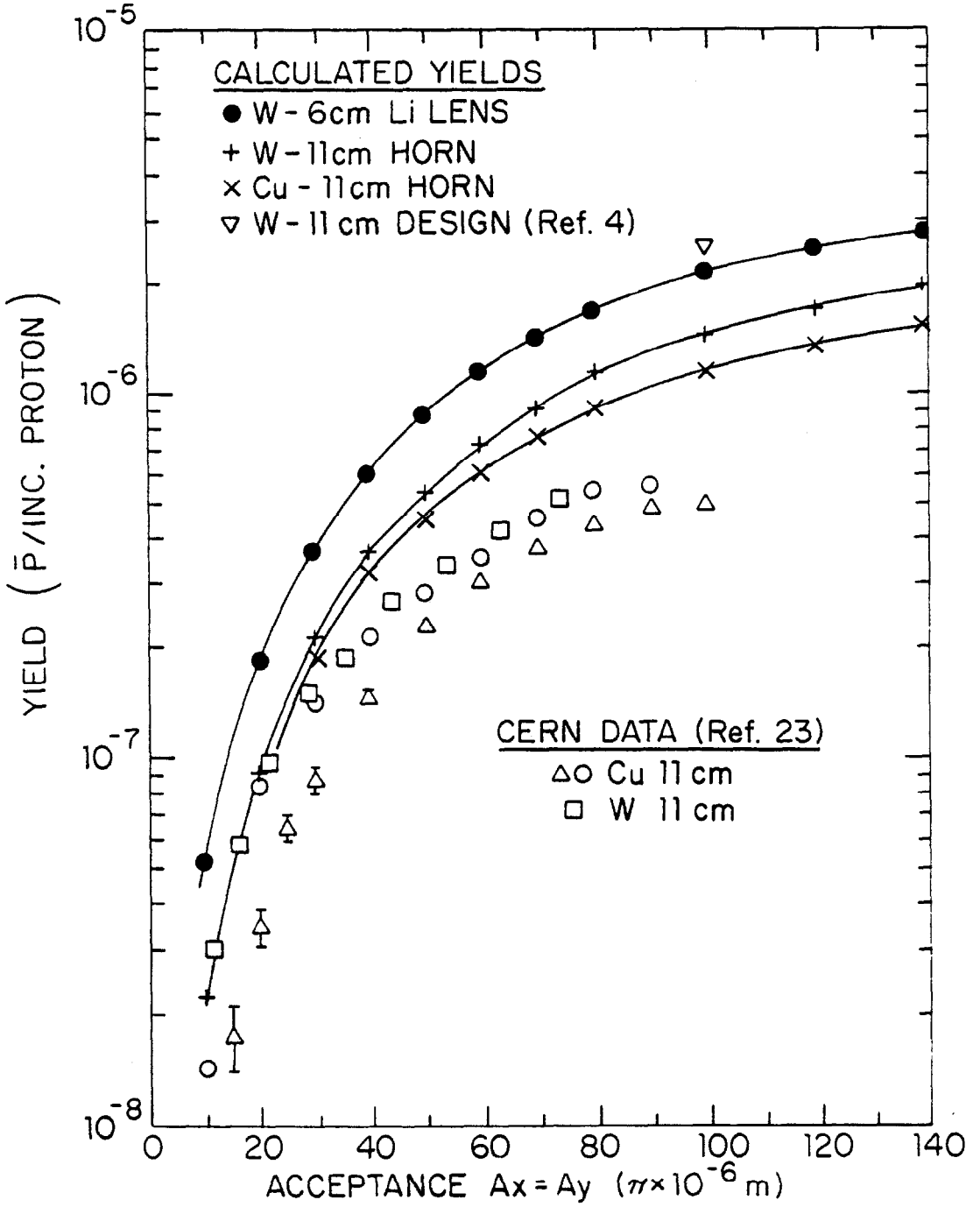
CALCULATED YIELDS
● W - 6cm Li LENS
+ W - 11cm HORN
× Cu - 11cm HORN
▽ W - 11 cm DESIGN (Ref. 4)
CERN DATA (Ref. 23)
△○ Cu 11 cm
□ W 11 cm
YIELD ($\bar{P}$/INC. PROTON)
10^{-5}
10^{-6}
10^{-7}
10^{-8}
0
20
40
60
80
100
120
140
ACCEPTANCE Ax = Ay ($\pi \times 10^{-6}$ m)

FIGURE 29